In-Flight Aeroelastic Stability of the Thermal Protection System on the NASA HIAD, Part II: Nonlinear Theory and Extended Aerodynamics

Benjamin D. Goldman* and Earl H. Dowell†
Duke University, Durham, NC, 27708, USA

Robert C. Scott‡
NASA Langley Research Center, Hampton, VA, 23681, USA

Conical shell theory and a supersonic potential flow aerodynamic theory are used to study the nonlinear pressure buckling and aeroelastic limit cycle behavior of the thermal protection system for NASA's Hypersonic Inflatable Aerodynamic Decelerator. The structural model of the thermal protection system consists of an orthotropic conical shell of the Donnell type, resting on several circumferential elastic supports. Classical Piston Theory is used initially for the aerodynamic pressure, but was found to be insufficient at low supersonic Mach numbers. Transform methods are applied to the convected wave equation for potential flow, and a time-dependent aerodynamic pressure correction factor is obtained. The Lagrangian of the shell system is formulated in terms of the generalized coordinates for all displacements and the Rayleigh-Ritz method is used to derive the governing differential-algebraic equations of motion. Aeroelastic limit cycle oscillations and buckling deformations are calculated in the time domain using a Runge-Kutta method in MATLAB.

Three conical shell geometries were considered in the present analysis: a 3-meter diameter 70° cone, a 3.7-meter 70° cone, and a 6-meter diameter 70° cone. The 6-meter configuration was loaded statically and the results were compared with an experimental load test of a 6-meter HIAD. Though agreement between theoretical and experimental strains was poor, the circumferential wrinkling phenomena observed during the experiments was captured by the theory and axial deformations were qualitatively similar in shape. With Piston Theory aerodynamics, the nonlinear flutter dynamic pressures of the 3-meter configuration were in agreement with the values calculated using linear theory, and the limit cycle amplitudes were generally on the order of the shell thickness. The effect of axial tension was studied for this configuration, and increasing tension was found to decrease the limit cycle amplitudes when the circumferential elastic supports were neglected, but resulted in more complex behavior when the supports were included. The nominal flutter dynamic pressure of the 3.7-meter configuration was significantly lower than that of the 3-meter, and it was found that two sets of natural modes coalesce to flutter modes near the same dynamic pressure. This resulted in a significant drop in the limit cycle frequencies at higher dynamic pressures, where the flutter mode with the lower frequency becomes more critical. Pre-buckling pressure loads and the aerodynamic pressure correction factor were studied for all geometries, and these effects resulted in significantly lower flutter boundaries compared with Piston Theory alone. The maximum dynamic pressure predicted by aerodynamic simulations of a proposed 3.7-meter HIAD vehicle was still lower than any of the calculated flutter dynamic pressures, suggesting that aeroelastic effects for this vehicle are of little concern.

*PhD candidate, Department of Mechanical Engineering and Materials Science, Box 90300 Hudson Hall, Student Member AIAA
†William Holland Professor, Department of Mechanical Engineering and Materials Science, Box 90300 Hudson Hall, Honorary Fellow AIAA
‡Sr. Aerospace Engineer, Aeroelasticity Branch, Associate Fellow AIAA

Nomenclature

a_∞	Speed of sound, m/s
a_{mn}, b_{mn}, c_{mn}	Modal coordinates for the three shell displacements
$\vec{a}, \vec{b}, \vec{c}$	Modal coordinates for the three shell displacements, in vector form
D_y, D_θ	Shell Bending stiffness in the y and θ directions, respectively, $Pa\ m^3$
$D_{y\theta}$	Shell in-plane twisting stiffness, $Pa\ m^3$
E_y, E_θ	Shell Young's Modulus in the y and θ directions, respectively, Pa
f	Frequency, Hz
f_{crit}	Critical frequency, at the flutter or divergence boundary, Hz
$G_{y\theta}$	Shear modulus, Pa
h	Shell thickness, m
I_n	Modified Bessel function of the first kind
k_s	Elastic support stiffness, N/m
K_n	Modified Bessel function of the second kind
m	Shell mass per area, kg/m^2, or the axial mode number
m_{tot}	Total number of axial modes
M_L	Local Mach number
$\hat{n}$	Circumferential mode number
n	$\hat{n}/sin\alpha$
n_{tot}	Total number of circumferential modes
n_{crit}	Critical circumferential mode number, at the flutter or divergence boundary
N_y^a	Tension forces in the y-direction, N/m
N_y^*	$-tan\beta p_s/2$
$N_{y,tot}^a$	Total in-plane force in y-direction (due to pressure and tension), N/m
N_θ^*	$-tan\beta p_s$
$N_{\theta,tot}^a$	Total applied in-plane force in θ-direction, N/m
p	Temporal Laplace transform variable
p_s	Static pressure differential, Pa
$q_{A,L}$	Local dynamic pressure, Pa
$q_{A,Lcrit}$	Critical local dynamic pressure, at the flutter or divergence boundary, Pa
r	Cylindrical shell radial coordinate, m
R	Average radius of the cylindrical or conical shell, m
$\tilde{r}$	$r\delta$
s	Spatial Laplace transform variable
u, v, w	Shell displacements, m
w^{**}	Double Laplace transform of the deflection with respect to space and time
U_∞	Free-stream flow velocity, m/s
x	Cylindrical shell axial coordinate
y	Coordinate along the shell meridian
y_1, y_2	Locations of the shell minor and major ends, respectively
$\bar{y}$	Dimensionless shell coordinate, $(y - y_1)/(y_2 - y_1)$
α	Fourier transform variable ($s = i\alpha$)
β	Shell half-cone angle
α_m, β_m	Shell in-plane modal functions
δ	$\sqrt{(M^2(s + p/U_\infty)^2 - s^2)}$
Δp	Unsteady aerodynamic pressure
$\Delta p^{*\alpha}$	Spatial Laplace transform of the pressure
Δp^{**}	Double Laplace transform of the pressure with respect to space and time
$\epsilon_y, \epsilon_\theta, \epsilon_{y\theta}$	Middle surface strains in the y, θ, $y\theta$ directions, respectively
χ_y, χ_θ, $\chi_{y\theta}$	Middle surface curvatures in the y, θ, $y\theta$ directions, respectively
θ	Shell circumferential coordinate
ϕ	$\theta sin\alpha$, or the circumferentially dependent velocity potential

Φ	Circumferentially independent velocity potential
Φ^{**}	Double Laplace transform of the velocity potential, with respect to space and time
ψ_m	Shell axial modal function
γ	$R\delta$
ν_y, ν_θ	Poisson's ratio in the y and θ directions, respectively
τ	Temporal integration variable

I. Introduction

The purpose of this report series, consisting of the current work and reference [1], is to characterize the in-flight aeroelastic behavior of a proposed thermal protection system[2] for the NASA Hypersonic Inflatable Aerodynamic Decelerator (HIAD).[3] The HIAD is an inflatable aeroshell with a diameter significantly larger than that of current rigid aeroshells. Its size is not limited by the launch vehicle shroud, allowing heavier payloads to be delivered to higher elevations of planets like Mars. The HIAD is composed of two separate but interacting structural components: a stacked inflatable toroid substructure and a thermal protection system (TPS). An illustration of these components is shown in Fig. 1, for the 3-meter diameter HIAD used in the Inflatable Re-Entry Vehicle Experiment.[4] The TPS is flexible enough to be packed into a small volume for transport and expands with the inflation of the toroid substructure in space. As a result of this flexibility, the TPS may be susceptible to static or dynamic aeroelastic instabilities such as "divergence" (buckling) or "flutter," which may be induced by fluid-structure interaction during atmospheric re-entry.

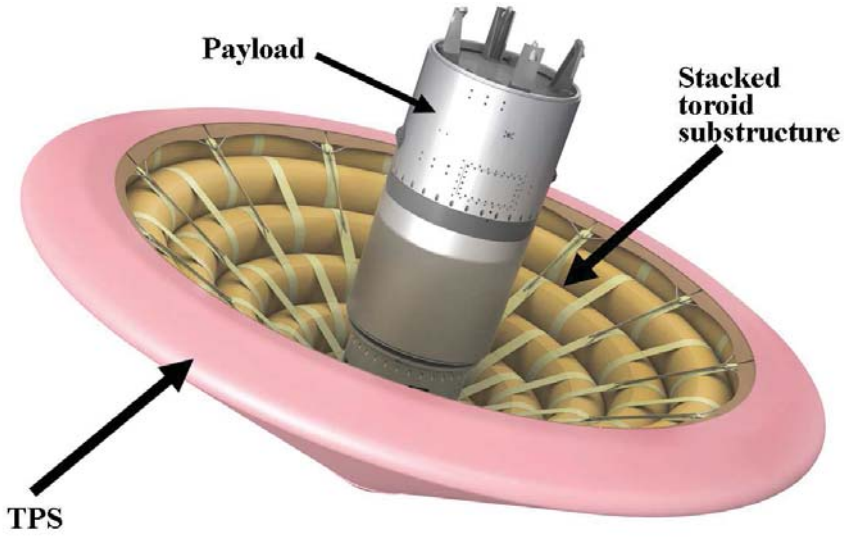

Figure 1: Illustration of the HIAD used in the Inflatable Re-Entry Vehicle Experiment.[4]

As a first attempt at characterizing the aeroelastic behavior of this system, experimental aerothermal performance tests[2,5] were conducted on small rectangular TPS coupons in the NASA 8' High Temperature Tunnel. Observations of oscillatory motion and failure of these samples during testing suggested that aeroelastic effects needed additional study, and theoretical model development was required. Goldman, Dowell, and Scott[6,7] developed several theoretical aeroelastic models for the TPS coupons, and agreement between theory and experiment for select cases was achieved. A rough prediction of in-flight stability can be made from these plate-like models; however, more precise predictions require structural models consistent with the in-flight TPS geometry, i.e. that of one or more conical shells.

In Part I[1] of this report series, linearized conical shell theory and Piston Theory aerodynamics were used to determine the aeroelastic stability boundaries for the TPS on the 3-meter HIAD. Several aeroelastic models were developed, and in most cases, flutter was found to be the primary instability. The limitations

of linear theory did not allow the amplitude of flutter oscillations to be determined, and the nonlinear effect of static pressure was ignored. Pressure-induced buckling was not studied since the buckling pressures predicted by linear theory were orders of magnitude lower than the pressures seen in flight. In the current analysis, nonlinear conical shell theory is used to study the buckling and aeroelastic limit cycle oscillations over a range of dynamic pressures above the linear flutter boundary. The initial deformation caused by the static pressure loading is also included. An extended aerodynamic theory is also developed to study more accurately the aeroelastic behavior in Mach number regimes where Piston Theory is less accurate.

II. Background and Previous Work

Details on the thermal protection system modeling can be found in reference [1]. A brief summary of the structural models and TPS will be provided here, since the current analysis is based on the previous work. The generation 1 TPS configuration[2] consists of one layer of Aluminized Kapton Kevlar (AKK), four layers of Pyrogel 2250, and two layers of Nextel 440-BF20. The AKK is composed of Kevlar woven fabric, coated with thin layers of Aluminum and Kapton. The Pyrogel is a soft sponge-like insulator, which ensures heating of the AKK is low enough to prevent structural failure. The Nextel is a woven fabric thermal barrier that takes most of the heat load. This system of interacting layers has been simplified for computational efficiency and can be approximated as a shell-like structure. Three structural models have been developed, and engineering illustrations are given in Fig. 2.

The single shell model consists of a single truncated conical shell. The separate layers of the thermal protection system are approximated as a single layer of AKK with added mass to account for the Nextel and Pyrogel. Tension in the axial direction can also be applied at the shell boundaries. The boundaries are simply-supported in all three shell displacement directions.

The elastically supported single shell model consists of a truncated conical shell with six middle surface circumferential elastic supports. These supports take into account the presence of the HIAD's toroid substructure, in a linear sense. As in the previous case, the three separate layers of the TPS are approximated as a single layer of AKK with added mass for the Nextel and Pyrogel, tension can be applied, and the boundary conditions remain the same.

The elastically supported three-layer shell model consists of one AKK shell and one Nextel shell separated by a Pyrogel linear elastic layer. The Nextel shell is one layer of Nextel material with twice the nominal mass, as two layers of Nextel are stitched together in the TPS. Since the Pyrogel is a soft, sponge-like material, it is approximated as a linear elastic layer. This layer is assumed to be bonded to the top and bottom of the AKK and Nextel surfaces, respectively. The boundary conditions are the same for all layers, and are identical to the previous two cases.

The linear aeroelastic equations of motion corresponding to each of the structural models above were derived using the Rayleigh-Ritz method with a Lagrangian in terms of the generalized coordinates for all shell displacements. The aerodynamic pressure is given by cylindrical shell Piston Theory,[8] and included in the equations as generalized forces. Aeroelastic solutions were obtained by writing the equations as an eigenvalue problem, and observing the behavior of the eigenvalues and eigenvectors with increasing flow dynamic pressure. Since a linear structural theory is employed, only the stability boundaries could be determined using this method. The critical modes and dynamic pressures obtained from the eigenanalysis will be necessary to simplify greatly the nonlinear calculations and reduce computation time.

III. Nonlinear Methods

The goal of the current work is to study the nonlinear pressure-buckling and aeroelastic response of the TPS structural models developed in Part I[1] of this report series. Since the nonlinear problem is substantially more complex, only the single shell (A) and elastically-supported single shell (B) models will be considered here. Additionally, for the purposes of determining the worst-case scenario for flutter and LCO, further analysis of model C is unnecessary since linear theory predicts the flutter boundaries for this case to be nearly an order of magnitude larger than models A and B.

The nonlinear equations of motion are derived from the full Donnell strain-displacement relations and

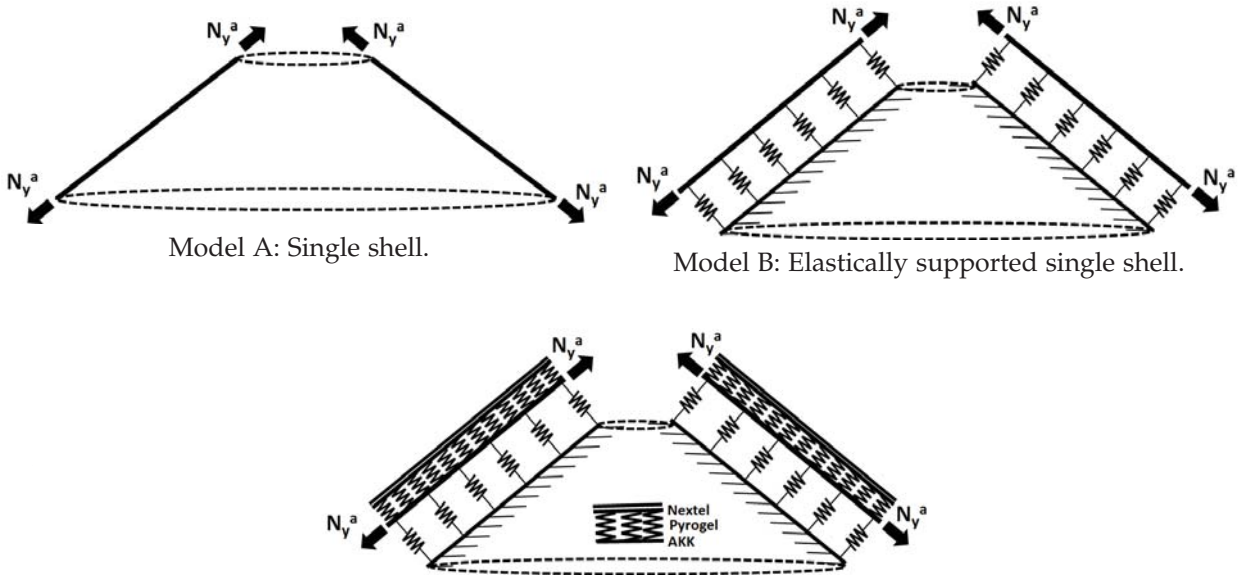

Model A: Single shell.

Model B: Elastically supported single shell.

Model C: Elastically supported three-layer shell
(not considered in the nonlinear analysis).

Figure 2: Conical shell structural models of the TPS.

the Rayleigh-Ritz is employed. A time-integration procedure has been developed to solve the resulting set of coupled differential-algebraic equations. Typical results for the full nonlinear aeroelastic system include limit cycle oscillations (LCOs), in which the flutter amplitude grows initially but is limited by the nonlinearities in the structure. Frequency spectra and time-dependent deflection shapes can also be calculated using this method. The proposed nonlinear analysis is advantageous because the magnitude of flutter oscillations can be determined, which may be necessary for fatigue analyses of the TPS materials. The static shape and strain distribution of the shells at pressures higher than the linear buckling pressure can also be determined and compared with experimental static load tests.

III.A. Nonlinear Aeroelastic Equations of Motion

The first step in applying the Rayleigh-Ritz method is to derive the total strain and elastic potential energy, kinetic energy, and non-conservative virtual work for the nonlinear shell system. To form the strain energies, the strain-displacement, stress-strain, and moment-curvature relations are needed.

The nonlinear Donnell strain-displacement relations given by Seide[9] are used here:

$$\begin{aligned} \varepsilon_y &= \frac{\partial u}{\partial y} + \frac{1}{2}\left(\frac{\partial w}{\partial y}\right)^2 \\ \varepsilon_\theta &= \frac{u - w\cot\beta}{y} + \frac{1}{y}\frac{\partial v}{\partial \phi} + \frac{1}{2y^2}\left(\frac{\partial w}{\partial \phi}\right)^2 \\ \varepsilon_{y\theta} &= \frac{\partial v}{\partial y} - \frac{v}{y} + \frac{1}{y}\frac{\partial u}{\partial \phi} + \frac{1}{y}\frac{\partial w}{\partial y}\frac{\partial w}{\partial \phi} \end{aligned} \tag{1}$$

The curvatures are linear functions of deflection (and its derivatives):

$$\begin{aligned} \chi_y &= \frac{\partial^2 w}{\partial y^2} \\ \chi_\theta &= \frac{1}{y}\frac{\partial w}{\partial y} + \frac{1}{y^2}\frac{\partial^2 w}{\partial \phi^2} \\ \chi_{y\theta} &= \frac{1}{y}\frac{\partial^2 w}{\partial y \partial \phi} - \frac{1}{y^2}\frac{\partial w}{\partial \phi} \end{aligned} \tag{2}$$

The force and moment relations are:

$$\begin{aligned} N_y &= \tfrac{E_y h}{1-\nu_y \nu_\theta}\left(\varepsilon_y + \nu_\theta \varepsilon_\theta\right) \\ N_\theta &= \tfrac{E_\theta h}{1-\nu_\theta \nu_y}\left(\varepsilon_\theta + \nu_y \varepsilon_y\right) \\ N_{y\theta} &= G_{y\theta} h \varepsilon_{y\theta} \end{aligned} \tag{3}$$

$$\begin{aligned} M_y &= -D_y\left(\chi_y + \nu_\theta \chi_\theta\right) \\ M_\theta &= -D_\theta\left(\chi_\theta + \nu_y \chi_y\right) \\ M_{y\theta} &= -D_{y\theta} \chi_{y\theta} \end{aligned} \tag{4}$$

The three shell displacements are expanded using modal series with summations over both the axial and circumferential modes. A double summation is necessary since the structural nonlinearities introduce coupling among the circumferential modes, which were previously uncoupled in the linear analysis. Note that these expansions only allow for standing waves along the shell circumference. The axial modes may be any functions that satisfy the geometric boundary conditions. Sine functions are used for simply-supported boundaries, where all three displacements vanish at the shell edges. The modal expansions are:

$$\begin{aligned} u(y,\theta,t) &= \sum_m \sum_n a_{mn}(t) \cos n\phi \psi_m(y) \\ v(y,\theta,t) &= \sum_m \sum_n b_{mn}(t) \sin n\phi \psi_m(y) \\ w(y,\theta,t) &= \sum_m \sum_n c_{mn}(t) \cos n\phi \psi_m(y) \end{aligned} \tag{5}$$

The strain energy is constructed by integrating over the entire shell surface the forces times strains and moments times curvatures:

$$U_S = \frac{1}{2}\int_{y_1}^{y_2}\int_0^{2\pi}\left(N_y\varepsilon_y + N_\theta\varepsilon_\theta + N_{y\theta}\varepsilon_{y\theta} - M_y\chi_y - M_\theta\chi_\theta - 2M_{y\theta}\chi_{y\theta}\right) y\, d\phi\, dy \tag{6}$$

The membrane energy associated with static axial or pressure loading is given by McNeal:[10]

$$U_{IS} = \frac{1}{2}\int_{y_1}^{y_2}\int_0^{2\pi}\left(N^a_{y,tot}\Theta_\theta^2 + N^a_{\theta,tot}\Theta_y^2 + \left\{N^a_{y,tot} + N^a_{\theta,tot}\right\}\Theta_n^2\right) y\, d\phi\, dy \tag{7}$$

where the strain rotation vectors are:

$$\begin{aligned} \Theta_\theta &= -\tfrac{\partial w}{\partial y} \\ \Theta_y &= \tfrac{v}{y\tan\beta} - \tfrac{1}{y}\tfrac{\partial w}{\partial \phi} \\ \Theta_n &= \tfrac{v}{2y} + \tfrac{1}{y}\tfrac{\partial v}{\partial y} - \tfrac{1}{2y}\tfrac{\partial u}{\partial \phi} \end{aligned} \tag{8}$$

The total applied in-plane forces are related to the static pressure and tension by the relation:

$$\begin{aligned} N^a_{y,tot} &= -\tfrac{y\tan\beta p_s}{2} - N^a_y \\ N^a_{\theta,tot} &= -y\tan\beta p_s \end{aligned} \tag{9}$$

A derivation of the relationship between in-plane forces and the externally-applied static pressure can be found in the appendix.

The toroid foundation on the HIAD is approximated by several linear circumferential elastic supports. The elastic potential energy for these supports is:

$$U_{ES} = \frac{k_s}{2}\int_0^{2\pi\sin\beta}\sum_i w^2\, y\big|_{y=y_i}\, d\phi \tag{10}$$

where y_i refers to the elastic support location along the shell middle surface.

The total kinetic energy, neglecting rotatory inertia, is:

$$T = \frac{m}{2}\int_{y_1}^{y_2}\int_0^{2\pi}\left[\left(\frac{\partial u}{\partial t}\right)^2 + \left(\frac{\partial v}{\partial t}\right)^2 + \left(\frac{\partial w}{\partial t}\right)^2\right] y d\phi dy \tag{11}$$

The virtual work and generalized forces are:

$$\delta W = -\int_0^{2\pi \sin\alpha}\int_{y_1}^{y_2}(\Delta p + p_s)\delta w y d\phi dy \tag{12}$$

$$Q_{mnsk} = \int_0^{2\pi \sin\alpha}\int_{y_1}^{y_2}((\Delta p)_{sk} + p_s)\mathrm{cosn}\phi\psi_m y d\phi dy \tag{13}$$

where $(\Delta p)_{sk}$ is the modal form of the aerodynamic pressure.

These generalized forces include the unsteady aerodynamic pressure as well as static pressure due to the mean flow, which is known from static CFD computations[11] of the HIAD vehicle. In most cases, Piston Theory will be used for the aerodynamic pressure. In the next section, an extended aerodynamic theory will be developed that will modify significantly the form of the aerodynamic generalized forces.

After substituting Eq. 5 into Eqs. 6 - 12, constructing the Lagrangian, and applying the Lagrange equation for each modal coordinate, a large system of ordinary differential equations is obtained for all three shell displacements. This system of equations is difficult to solve because the in-plane frequencies for shells are often orders of magnitude higher than out-of-plane deflection frequencies, requiring a very small time step in the computational scheme. However, since the in-plane inertia is small relative to the out-of-plane inertia, it may be neglected. This requires that the following linear system involving the in-plane coordinates be solved at every time step :

$$\begin{bmatrix} \boldsymbol{A} + \boldsymbol{A}^T + \left(N_y^* + N_\theta^*\right)\left(\boldsymbol{N} + \boldsymbol{N}^T\right) & \boldsymbol{B} + \left(N_y^* + N_\theta^*\right)\boldsymbol{O}^T \\ \boldsymbol{B}^T + \left(N_y^* + N_\theta^*\right)\boldsymbol{O} & \boldsymbol{C} + \boldsymbol{C}^T + \left(N_y^* + N_\theta^*\right)\left(\boldsymbol{PP} + \boldsymbol{PP}^T\right) + N_\theta^*\left(\boldsymbol{QQ} + \boldsymbol{QQ^T}\right) \end{bmatrix} \begin{Bmatrix} \vec{a} \\ \vec{b} \end{Bmatrix} = -\begin{Bmatrix} \boldsymbol{D}\vec{c} + \boldsymbol{C}\vec{\boldsymbol{C}}\boldsymbol{J} \\ \boldsymbol{E}\vec{c} + \boldsymbol{C}\vec{\boldsymbol{C}}\boldsymbol{L} + N_\theta^*\boldsymbol{R}\vec{c} \end{Bmatrix} \tag{14}$$

Along with the ODE for $\vec{c}$:

$$\begin{aligned}\left[\boldsymbol{I} + \boldsymbol{I}^T\right]\ddot{\vec{c}} = &-\left(\boldsymbol{D}^T\vec{a} + \boldsymbol{E}\vec{b} + \left[\boldsymbol{F} + \boldsymbol{F}^T\right]\vec{c}\right) + \vec{Q}^A + \boldsymbol{ES}\vec{c} \\ &+N_\theta^*\left(\boldsymbol{R}^T\vec{b} + \left(\boldsymbol{S} + \boldsymbol{S}^T\right)\vec{c}\right) + N_y^*\left(\boldsymbol{T} + \boldsymbol{T}^T\right)\vec{c} + \boldsymbol{C}\vec{\boldsymbol{C}}\boldsymbol{C}\end{aligned} \tag{15}$$

The full expressions for the vectors and coefficient matrices in the equations above are provided in the appendix. Note that the right-hand-side of Eq. 14 is a nonlinear function of the deflection coordinate $\vec{c}$, but the system is linear with respect to the in-plane coordinates $\vec{a}$ and $\vec{b}$. This method, in which Eq. 14 is solved at every time-step, was found to be nearly one order of magnitude faster than solving the full system including in-plane inertia. An analysis with 12 axial and 2 circumferential modes was performed, and it was found that in-plane inertia had little effect on both the flutter boundaries and LCO amplitudes.

Nonlinear aeroelastic solutions are calculated by first performing the linear analysis described in Part I.[1] Linear theory predicts a single critical circumferential mode as well as coalescence of two axial modes at the flutter dynamic pressure. A nonlinear time integration simulation is then performed with initial conditions (displacements) in the coordinates for these critical modes only. It was found that the system is generally not sensitive to the magnitude of the initial conditions, and giving initial conditions in non-critical modes also produces the same results, but additional computation time is then required to reach a steady state. Additionally, at least two circumferential modes are needed to introduce coupling in the nonlinear terms such that they are nonzero (the only exception to this is if n_{crit}=0.)

III.B. Extended Potential Flow Aerodynamic Theory

Since the local flow solution behind the HIAD's bow shock is known from static CFD simulations,[11] Piston Theory can be used as an initial approximation for the aerodynamic pressure. This approach has been used in several previous works on conical shell flutter, including Dixon and Hudson[12] and Mahmoudkhani et al.[13] Krumhaar[8] derived a Piston Theory curvature correction term for cylindrical shells, which can be easily modified for the conical shell by letting $R = ysin\beta$. The "corrected" piston theory used for most computations in this paper is given by:

$$\Delta p = \frac{2q_{A,L}}{M_L}\left[\frac{\partial w}{\partial y} + \frac{1}{U_\infty}\frac{\partial w}{\partial t} - \frac{1}{2M_L}\frac{w}{y\sin\beta}\right] \tag{16}$$

Piston Theory is a convenient tool for aeroelastic computations, since it can be included directly into the structural equations of motion as generalized forces, independent of temporal or spacial memory. However, as the Mach number approaches 1 supersonically, this approximation may no longer be sufficient. Generally $M^2 >> 1$ is the necessary condition for validity.[14] Since the maximum local Mach number on the HIAD surface is approximately 1.5 - 2, investigation into a more elaborate aerodynamic theory is needed. Full potential flow theory is the next level of approximation, but a direct solution using transform methods is cumbersome and difficult, especially when performing the inversion of transform integrals. Following the method of Dowell and Bliss for 2-D airfoils,[15] Potential Flow theory can be used to extend conical shell Piston Theory to a lower Mach number range by expanding the transform of the aerodynamic pressure in powers of inverse Mach number. Under the local flow assumption, we start by transforming the convected wave equation for potential flow in cylindrical coordinates with respect to both time and the streamwise coordinate x:

$$\mathcal{L}_s\mathcal{L}_p\left[\frac{1}{r}\frac{\partial\Phi}{\partial r} + \frac{\partial^2\Phi}{\partial r^2} - \frac{n^2}{r^2}\Phi + \frac{\partial^2\Phi}{\partial x^2} - \frac{1}{a_\infty^2}\left(\frac{\partial^2\Phi}{\partial t^2} + 2U_\infty\frac{\partial^2\Phi}{\partial x\partial t} + U_\infty^2\frac{\partial^2\Phi}{\partial x^2}\right)\right] \tag{17}$$

where $\phi(x,r,\theta,t) = \Phi(x,r,t)\cos n\phi$. The transforms result in the following modified Bessel equation:

$$\tilde{r}^2\frac{\partial^2\Phi^{**}}{\partial\tilde{r}^2} + \tilde{r}\frac{\partial\Phi^{**}}{\partial\tilde{r}} - \left[n^2 + \tilde{r}^2\right]\Phi^{**} = 0 \tag{18}$$

where $\tilde{r} = r\delta$, $\delta^2 = M^2\left(s + \frac{p}{U_\infty}\right)^2 - s^2$, and the double Laplace transform of the potential is:

$$\Phi^{**} = \int_0^\infty\int_0^\infty \Phi(x,r,t)e^{-sx-pt}dxdt \tag{19}$$

The general solution to Eq. 18 is a linear combination of modified Bessel functions:

$$\Phi^{**} = c_1 I_n(\tilde{r}) + c_2 K_n(\tilde{r}) \tag{20}$$

and after applying the finiteness condition as r approaches infinity,

$$\Phi^{**} = c_2 K_n(\tilde{r}) \tag{21}$$

The boundary condition at all points along the shell axis requires that the local velocity on the shell surface be equal to the downwash:

$$\left.\frac{\partial\phi}{\partial r}\right|_{r=R} = U_\infty\frac{\partial w}{\partial x} + \frac{\partial w}{\partial t} \tag{22}$$

and the transform of this boundary condition is:

$$\left.\frac{\partial\Phi^{**}}{\partial\tilde{r}}\delta\right|_{\tilde{r}=R\delta} = (U_\infty s + p)\,w^{**} \tag{23}$$

After applying the transform of the boundary condition to the transform of the potential, the unknown coefficient c_2 can be determined. The complete expression for the transform of the potential is:

$$\Phi^{**} = \frac{K_n(\tilde{r})w^{**}}{K_n{}'(R\delta)\delta}\,(U_\infty s + p) \tag{24}$$

The pressure at every point along the shell axis is given by the Bernoulli equation:

$$\Delta p = -\rho \left(\frac{\partial \phi}{\partial t} + U_\infty \frac{\partial \phi}{\partial x} \right) \Bigg|_{r=R} \tag{25}$$

After taking the transform of Eq. 25 and using Eq. 24, the transform of the aerodynamic pressure is obtained:

$$\Delta p^{**} = -\rho R (p + U_\infty s)^2 w^{**} \left(\frac{K_n(\gamma)}{\gamma K_n{}'(\gamma)} \right) \tag{26}$$

where $\gamma = R\delta$. Following Krumhaar[8] and Bateman et al.,[16] the asymptotic expansion of the quantity in parentheses (for large γ) is:

$$\frac{K_n(\gamma)}{\gamma K_n{}'(\gamma)} = -\gamma^{-1} + \frac{1}{2}\gamma^{-2} + \left(\frac{n^2}{2} - \frac{3}{8} \right) \gamma^{-3} + ... \tag{27}$$

This expansion can be further simplified by applying the Dowell and Bliss method,[15] whereby algebraic manipulation is used to re-write each term in Eq. 27, and applying the binomial theorem. This procedure is outlined in the appendix. The resulting transform of the pressure, including terms up to $O(1/M^5)$ is:

$$\begin{aligned} \Delta p^{**} = \rho U_\infty^2 W^{**} \Bigg\{ & \frac{1}{M}\left(s + \frac{p}{U_\infty}\right) - \frac{1}{2RM^2} + \frac{s^2}{2M^3\left(s+\frac{p}{U_\infty}\right)} - \frac{\frac{n^2}{2}-\frac{3}{8}}{R^2M^3\left(s+\frac{p}{U_\infty}\right)} \\ & - \frac{s^2}{2RM^4\left(s+\frac{p}{U_\infty}\right)^2} - \frac{3\left(\frac{n^2}{2}-\frac{3}{8}\right)s^2}{2R^2M^5\left(s+\frac{p}{U_\infty}\right)^3} \Bigg\} \end{aligned} \tag{28}$$

The first two terms in Eq. 28 correspond to classical Piston Theory and Krumhaar's curvature correction factor. To form the aerodynamic generalized forces, the transform of the pressure must be inverted back to physical space and time. It is convenient; however, to bypass the spatial inversion of the pressure and instead invert the transform of the generalized forces in the following manner:

1. Invert Eq. 28 with respect to time. Requires a convolution integral of the spatial transform of deflection and the temporal exponential integrals.

2. Apply the Bromwich integral in Fourier space, using $s = i\alpha$ and $x = (y - y1)cos\beta$ (change of variable for conical shell reference frame):

$$\frac{\cos\beta}{2\pi} \int_{-\infty}^{\infty} \Delta p^{*\alpha} e^{i\alpha(y-y_1)\cos\beta} d\alpha \tag{29}$$

   Note that this integral is not calculated explicitly until step 4.

3. Perform all spatial integrations, including the transform of the deflection and the axial and circumferential integrals from Eq. 13.

4. Integrate with respect to α over the real infinite domain.

If the order of the above procedure is followed, only integration with respect to α and τ (temporal integration variable) must be computed numerically. The infinite limits for the integral with respect to α may be truncated based on how the integrand decays, which depends on the axial mode number, Mach number, speed of sound, and shell geometry. A plot of the integrand of the Kernel function vs. α is given in Fig. 3 for the 3.7 meter shell at Mach 2, with a_∞=340 m/s. For the first three modes shown, integration may be truncated at $\alpha = 30$, but limits must be extended for higher modes. The integrand of the Kernel function is always symmetric about $\alpha = 0$.

The resulting correction factor for the aerodynamic generalized forces is:

$$Q_{sk}^{A,\,corr} = 2q_A \cos\beta \sum_n \sum_m \Xi_{nk}^1 \int_0^t c_{mn}(t) A_{mnsk}(t-\tau) d\tau \tag{30}$$

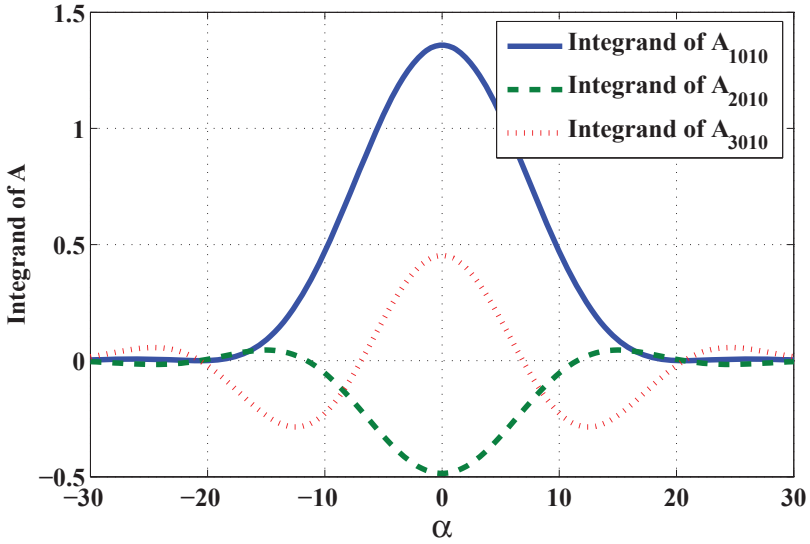

Figure 3: Integrand of the Aerodynamic kernel function vs. the Fourier variable α, 3.7-meter shell, $M_L = 2$, $a_\infty = 340\ m/s$.

The complete expression for the Kernel $A_{mnsk}(t)$ is given in the appendix. Note that since this expression is a function of the circumferential mode number, it is effectively a three-dimensional extension of Piston Theory.

Plots of the Kernel as a function of time are given in Fig. 4, showing the influence of the first three axial modes on the first axial mode. The Kernel decays rapidly to zero at a characteristic time that depends on the aerodynamic and structural parameters, but is mostly influenced by the Mach number. The case shown in Fig. 4 has the same parameters as Fig. 3. Here, the characteristic time is approximately 0.00068 seconds. This is the amount of deflection time history required for numerical bookkeeping in order to compute the convolution integral in Eq. 30.

IV. Results

Results are computed for a specific set of test cases developed in coordination with HIAD investigators at the NASA Langley Research Center. The first set of results are from validation studies, ensuring that the nonlinear buckling and aeroelastic simulations are consistent with the linear theory in Part I.[1] Next, deflection shapes and strains for a static load simulation are presented, corresponding to experimental tests performed on a 6-meter HIAD article. Aeroelastic limit cycle oscillations are then calculated for various cases, and the effects of axially-applied tension are examined for the 3-meter geometry. Finally, pre-buckling pressure loads and the extended potential flow aerodynamic model are included in the aeroelastic simulations and results are calculated for a 3.7-meter shell.

A summary of the numerical test cases studied in this paper (in the order presented) are given in Table 1. Simply-supported modal functions are used in all computations, as indicated by the "-1" identifier in the model description (see Part I[1]). Note that almost all of the cases presented are for model B, which is the elastically-supported conical shell. Results for model A, the single shell, are only included for comparison in the parameter study examining the effects of axially-applied tension.

IV.A. Verification, Convergence Studies and Linear/Nonlinear Model Comparison

To verify that the time-integration scheme has been implemented correctly, various comparisons were made with the linear theory used in Part I.[1] Note that this linear analysis was found to be consistent with previously published results on the free vibrations and flutter of conical shells.

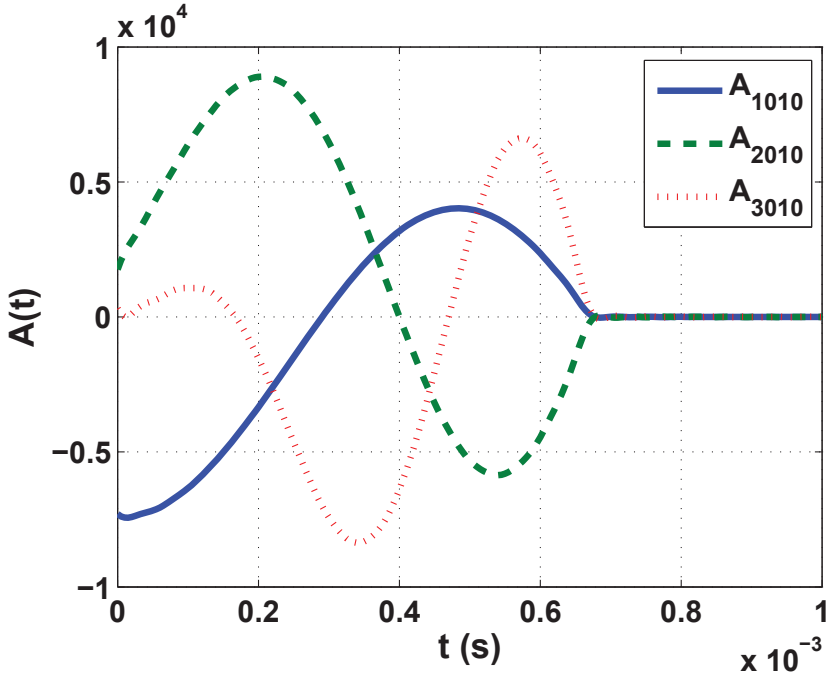

Figure 4: Aerodynamic kernel function vs. time, 3.7-meter shell, $M_L = 2$, $a_\infty = 340 m/s$.

Table 1: Numerical test case matrix.

Aeroelastic model	Geometry	p_s (Pa)	N_y^a (N/m)	M	Aerodynamics
B-1	6-meter, 70°	3000, 4500, 6000	0	0	None (static load)
A-1, B-1	3-meter, 70°	0	0, 250, 500, 750, 1000	2	Piston theory
B-1	3-meter, 70°	0, 1000	0	2	Piston theory
B-1	3.7-meter, 70°	0, 1000	0	2	Piston theory
B-1	6-meter, 70°	0, 1000	0	2	Piston theory
B-1	3-meter, 70°	0	0	2	Extended
B-1	3.7-meter, 70°	0	0	2	Extended
B-1	6-meter, 70°	0	0	2	Extended

First, a buckling analysis was computed in the time domain, using the critical circumferential buckling mode ($n_{crit} = 43$) found in the eigenanalysis (for the 6-meter configuration), and neglecting all nonlinear terms. The results, shown in Fig. 5, show that the amplitude of the buckling mode increases with time at the linear buckling pressure, and decays with time at lower pressures. While not a complete model validation, these results indicate that the new time-integration method is consistent with the previous linear analysis with respect to buckling.

To determine the number of modes required in the expansions for the shell displacements (Eq. 5), several convergence studies were performed. Convergence of the axial modes is shown in Fig. 6 for the nominal cases A-1 (single shell) and B-1 (elastically-supported single shell). A large number of circumferential modes were used to ensure convergence in the circumferential direction. Axial convergence is attained when the critical dynamic pressure no longer changes with the total number of axial modes. Case B-1 requires significantly more axial modes because the elastic supports along the shell middle-surface must be resolved. Note that axial mode convergence patterns for the linear and nonlinear methods are nearly identical. This is a result of the limited influence of structural nonlinearities near the flutter boundary.

Next, convergence of the circumferential modes was analyzed. Several nonlinear flutter calculations

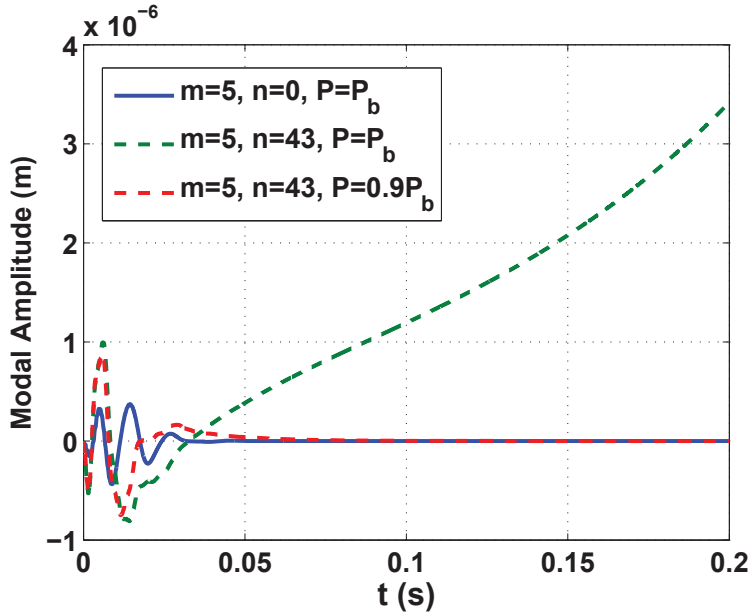

Figure 5: Verification of the time-integration method for calculating the linear buckling pressure.

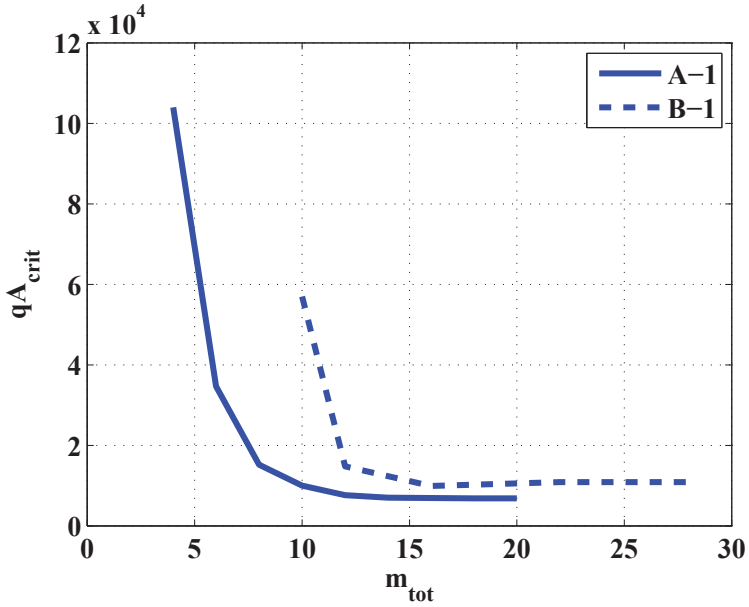

Figure 6: Axial modal convergence for the nonlinear aeroelastic models.

were performed with various combinations of axial and circumferential modes at different values of $q_{A,L}$, with M_L=2. One such calculation for case A-1 included 12 axial and 6 circumferential modes (n=0, 1, 2, 3, 4, 5), with $q_A = 8,000Pa$, 20% above the linear flutter dynamic pressure. Limit cycle oscillations (LCOs) were observed, with finite peak amplitudes on the order of the shell thickness. Examination of the modal coordinates indicated that only the critical flutter mode ($n_{crit} = 3$) and the symmetric mode ($n = 0$) are significant, with all other modes being several orders of magnitude lower. Table 2 illustrates this behavior. For conciseness, only data for critical axial modes (7 & 8) are shown. This suggests that only $n = n_{crit}$ and $n = 0$ are needed for a nonlinear aeroelastic analysis of the nominal single shell configuration. This is highly convenient, since an instantaneous linear analysis can be performed to

determined the circumferential mode needed for the nonlinear calculation (this would otherwise take orders of magnitude longer to compute in the time-domain). In case B-1, linear theory predicts that the axisymmetric mode ($n = 0$) is most critical. Thus, only this circumferential mode is needed for the nonlinear aeroelastic simulations for case B-1. Note: The nonlinear terms in the equations of motion vanish if only the critical circumferential mode is included. The critical mode must be coupled to the $n = 0$ mode for nonlinear terms to survive. The only exception to this rule is for $n = 0$, which has self-coupling and may be included without coupling to any other modes.

Table 2: Deflection modal coordinates for case A-1 as a function of axial and circumferential mode number - critical axial modes only.

m	n	c_{mn}
7	**0**	**3.07E-06**
7	1	5.14E-13
7	2	9.58E-12
7	**3**	**9.8E-05**
7	4	7.73E-12
7	5	2.43E-13
8	**0**	**2.99E-05**
8	1	2.25E-12
8	2	1.08E-11
8	**3**	**1.02E-4**
8	4	8.4E-12
8	5	2.12E-13

The limit cycle oscillations computed in the convergence study for case A-1 are given in Fig. 7. While an initial transient is present, the oscillations after t=1s are generally constant in amplitude and at a single frequency. An FFT of this time history, given in Fig. 8, shows that the frequency is approximately 1% higher than that predicted by linear theory (aerodynamic stiffening effects are likely responsible for this result). Minimal response is also seen at the 2^{nd} harmonic, a consequence of the structural nonlinearities in the system.

A comparison of the linear and nonlinear mode shapes is given in Fig. 9. Note that nonlinear theory can predict the magnitude of the mode shape (shown here as normalized by the shell thickness), while the mode shape resulting from linear theory is purely relative (shown here as normalized by the maximum deflection). In both cases, the maximum deflection occurs near the trailing edge of the shell. The nonlinear result indicates that at dynamic pressures near the flutter boundary, the flutter amplitudes are on the order of the shell thickness.These results suggest that the nonlinear method is consistent with the linear methods developed in Part I.

IV.A.1. Static Loading/Buckling

Experimental static load tests[17] of a 6-meter HIAD were conducted to simulate the pressure due to the mean flow during flight. This is illustrated in Fig. 10. A thin membrane was placed over the HIAD surface, sealed at the boundaries, and a vacuum was applied. This resulted in compression of TPS material between the inflated toroids, which is shown clearly in Fig. 10. A close inspection of the test article also revealed small wrinkles in the TPS along the axial direction of the article. Typically, wrinkling in shell-like structures indicates a buckling instability; however, once the pressure was relieved the TPS returned to its original undeformed shape, though some small wrinkles still remained. It is possible that the outermost fabric layer in the TPS relaxes as a result of the static deformation of the toroid substructure, causing wrinkles that are unrelated to buckling. Two types of nonlinear simulations can be used to characterize these experimental tests. First, a purely symmetrical analysis, that does not allow for any circumferential deformations, can be used to simulate the un-buckled but statically loaded state. Second, an asymmetrical

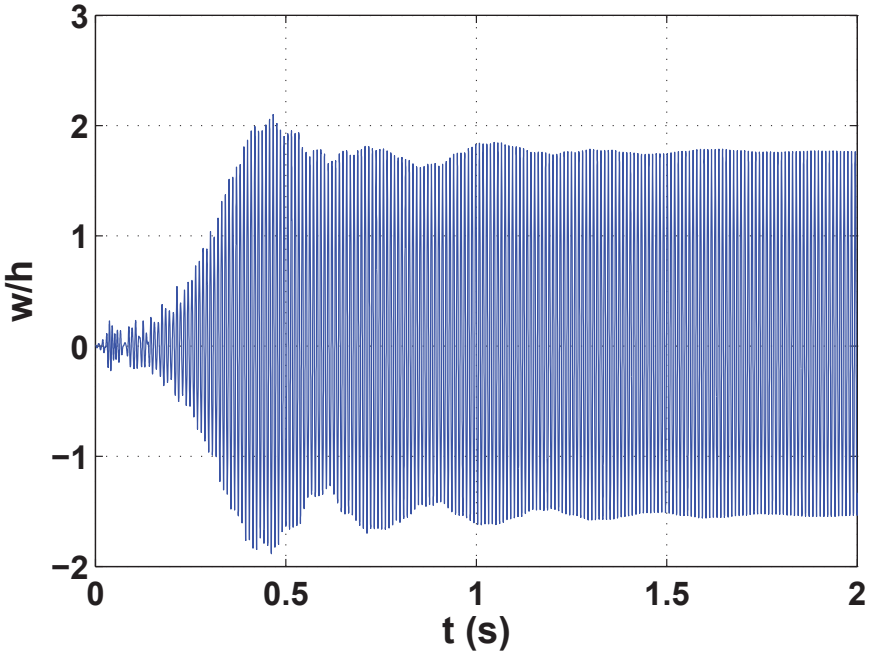

Figure 7: Limit cycle oscillations for the single shell model at M=2, q_A=8000 Pa, $\bar{y}$=0.95.

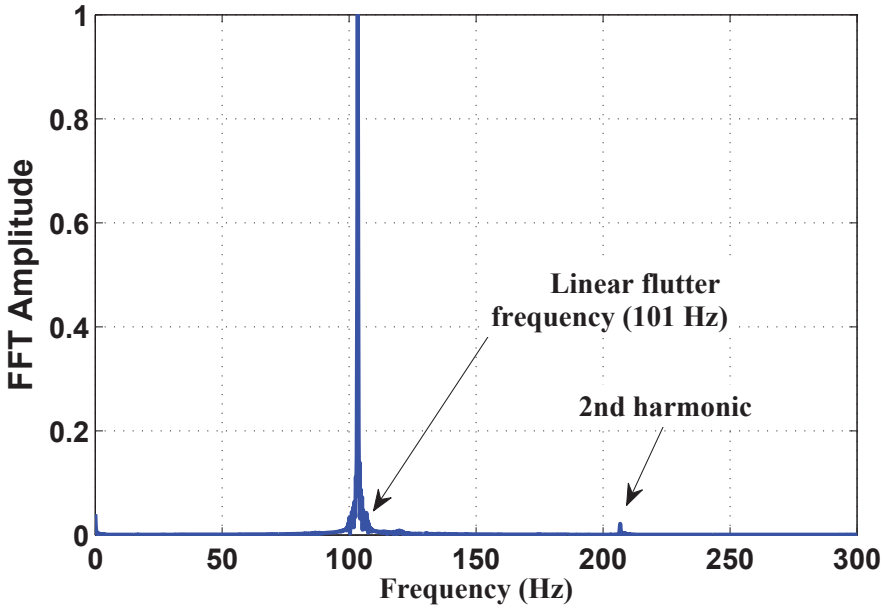

Figure 8: FFT of the limit cycle oscillations for the single shell model at M=2, q_A=8000 Pa, $\bar{y}$=0.95.

buckling analysis will determine the critical axial and circumferential buckling shape. In both cases, axial strain will be calculated near the major end of the shell and compared with experimental measurements.

The experimental article was loaded symmetrically with 3000, 4500, and 6000 Pascals of pressure and the strain was measured at different locations around the circumference using rosette gauges. For each loading condition, the toroid substructure was inflated with different pressures, resulting in slightly dif-

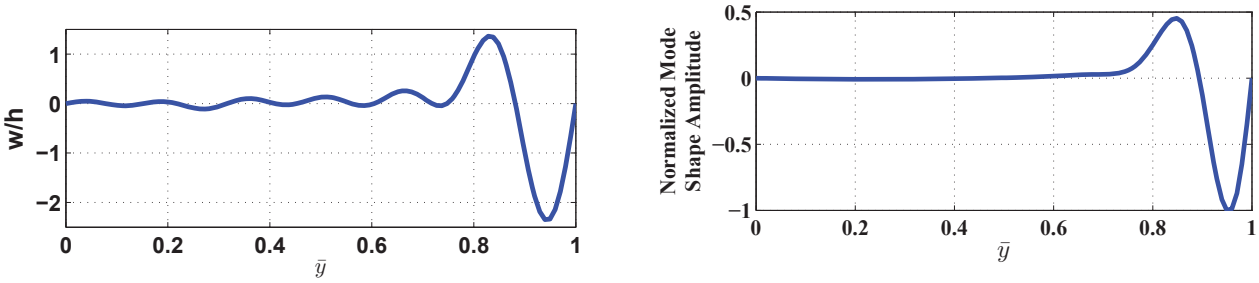

(a) Nonlinear flutter mode shape at M=2, q_A=8000 Pa.

(b) Linear flutter mode shape, M=2, q_A = 6728 Pa.

Figure 9: Comparison of the linear and nonlinear flutter mode shapes.

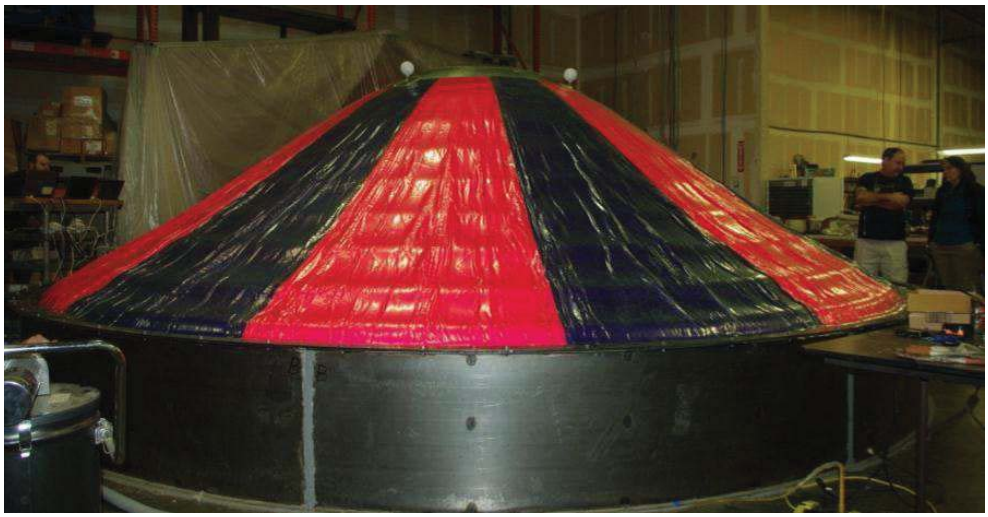

Figure 10: Experimental static load test of the 6-meter article.

ferent static deformations. For the purposes of this analysis, the effect of the substructure will be ignored and the average axial strain for all inflation pressures will be used for the comparison to theory. Additionally, despite being loaded symmetrically, imperfections in the structure resulted in highly asymmetric deformations, with strains being positive or negative depending on the location around the circumference. While the asymmetrical buckling analysis results in circumferentially-dependent strains, they are generally within a few percent of each-other. For comparison between theory and experiment, the circumferential dependence on strain will also be averaged out. These data are given in Table 3. The experimental results are approximately one order of magnitude larger than theory for each loading condition, though the general dependence on load is similar. When the buckling mode is included, the theoretical strains are larger but still significantly lower than the experiment. Better agreement between theory and experiment may be achieved by reducing the Young's Modulus in the simulations; however, this is inconsistent with the material property data given by the manufacturer.[18] It is more likely that the large static loads resulted in large deformations that are not in the regime of the current nonlinear shell theory. Note that in-flight static loads are significantly less than those applied to the test article (1000 Pa max), resulting in smaller deflections that should be within the regime of the current theory.

The axial and circumferential deflection patterns for the symmetric analysis with the 6000 Pa load are given in Figs 11 and 12, respectively. The maximum deflections are nearly 100 times the thickness of the shell, which in this particular case is about 1 centimeter. The deflections seen in Fig. 10 are clearly much larger than this, and consistent with the larger experimental strains. Qualitative agreement is seen in the axial behavior of the shell, with the largest deflections near the major end. Close inspection of the experimental article in Fig. 10 also indicates this behavior. Since the analysis is symmetric, the shell cross

section remains circular and no standing waves appear along the circumference.

Table 3: Theoretical and experimental microstrain as a function of static pressure load, measured between the last two toroids.

	Axial microstrain		
Load (Pa)	Experiment (average)	Theory (symmetric)	Theory (buckling, average)
3000	275	29	32
4500	439	44	55
6000	600	55	80

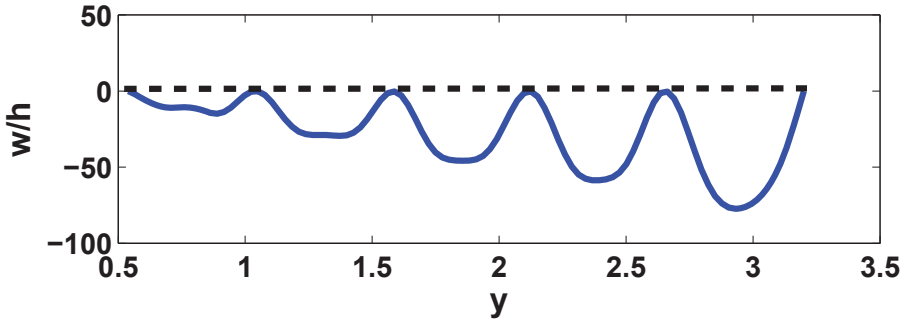

Figure 11: Axial deformation shape of the 6-meter article using a purely symmetrical analysis, $p_s = 6000Pa$. The dashed line indicates the undeformed shape.

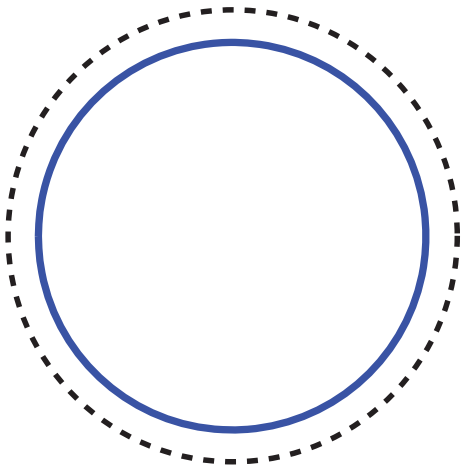

Figure 12: Circumferential deformation shape of the 6-meter article using a purely symmetrical analysis, $p_s = 6000Pa$. The dashed line indicates the undeformed shape.

The axial and circumferential deflection patterns for the asymmetrical analysis with the 6000 Pa load are given in Figs 13 and 14, respectively. The critical circumferential buckling mode ($n_{crit} = 43$) predicted by linear theory is included, and since the pressure here is larger than the critical nonlinear buckling pressure of 2000 Pa, the shell undergoes a bifurcation into a nonlinear buckling state. The maximum

axial deflections are larger than the symmetric case, though little deformation is seen before the last three toroids. Thi[illegible]ymmetrical analysis, th[illegible]waves seen in Fig. 14 is[illegible] Additional testing is ne[illegible]comparison to theory. It[illegible]e numerical results sug[illegible]r with high pressure.

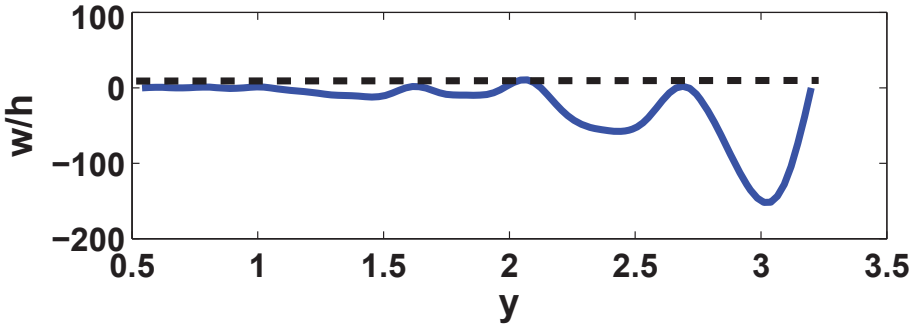

Figure 13: Axial deformation shape of the 6-meter article using an asymmetrical buckling analysis, $p_s = 6000\ Pa$. The dashed line indicates the undeformed shape.

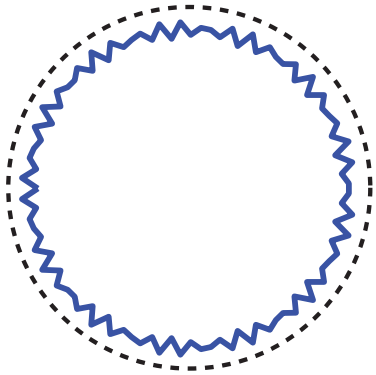

Figure 14: Circumferential deformation shape of the 6-meter article using an asymmetrical buckling anal-ysis, $p_s = 6000\ Pa$. The dashed line indicates the undeformed shape.

IV.A.2. Nominal Aeroelastic Cases

The nominal aeroelastic test cases are given in Table 4. Linear theory is used initially to determine the critical parameters at the flutter boundaries, including the dynamic pressure, circumferential mode, and frequency. The goal of the nominal cases is to establish baselines for flutter onset and characterize the effects of shell geometry, while also providing the necessary data for the subsequent nonlinear analyses. Recall that model A-1 is the single shell and model B-1 is the single shell with six elastic supports located at the approximate toroid positions on the HIAD. To reduce the complexity of these systems and allow for a more direct comparison between models, no tension or static pressure loading is included here. Conical shell Piston Theory is used for the aerodynamic pressure.

The results for model A-1 indicate that the flutter dynamic pressures and frequencies are inversely proportional to the shell radius. More specifically, the flutter dynamic pressures decrease proportional to the inverse square of the radius, while the frequency decreases proportional to the inverse of the radius.

If the quantity R/h were held constant in these computations, it is expected that the flutter dynamic pressure would scale with the inverse cube of the radius; however, the TPS thickness is independent of the HIAD geometry so the typical scaling laws do not hold. Note that the critical circumferential mode is independent of the shell radius (if the cone angle is held constant).

The results for model B-1 also show that the flutter dynamic pressures and frequencies are inversely proportional to the shell radius; however, the dynamic pressures decrease more rapidly with increasing radius than in model A-1. In this case, the flutter dynamic pressures decrease (approximately) proportional to $1/R^{2.33}$. If the quantities R/h and $k_s L^2/D_y$ were held constant, then the flutter dynamic pressure would scale with the inverse cube of the radius. The flutter frequencies are nearly identical to model A-1, which had been observed in the linear analysis in Part I[1] for the 3-meter geometry only. While the elastic supports seem to have little effect on the flutter frequencies, they do change the model coalescence behavior of the shell. For example, in the the 3.7-meter configuration (B-1), there is a second flutter mode with an infinitesimally higher flutter dynamic pressure that was not present in case A-1 with the same geometry. To investigate further this unusual behavior, additional calculations were performed using the linear methods. The natural frequencies and total system damping were calculated over a range of dynamic pressures until the flutter condition was attained, for the 3-meter and 3.7-meter geometries only. Two key properties of these frequencies are illustrated in Fig 15. First, the separation of the natural frequencies (at $q_A = 0$) is significantly decreased for the 3.7-meter compared to the 3-meter geometry, especially for the first several modes. Based on these data and additional calculations with larger diameter shells, it can be concluded that increasing the shell diameter reduces both the magnitude and separation of the modal frequencies, causing the flutter dynamic pressure to decrease. Second, Fig. 15 indicates that in the 3.7-meter configuration, modes 1+2 and 4+5 become unstable and coalesce at nearly the same dynamic pressure, while for the 3-meter case, only the first two modes are most critical. These coalescence points are indicated by "A" and "B" in Fig 15b for the 3.7-meter case only. Coalescence between the first two modes occurs at a slightly lower dynamic pressure, by fraction of a percent. These results will be important for the nonlinear analyses in section IV.A.5, where limit cycle frequencies shift between these two flutter modes depending on the dynamic pressure.

Table 4: Critical parameters for the nominal aeroelastic cases.

Model and Geometry	$\mathbf{q_{crit}}$ **(Pa)**	$\mathbf{n_{crit}}$	$\mathbf{f_{crit}}$ **(Hz)**	$\mathbf{M_L}$
A-1, 3-meter, 70°	6936	3	101	2
A-1, 3.7-meter, 70°	4620	3	82	2
A-1, 6-meter, 70°	1850	3	49	2
B-1, 3-meter, 70°	10866	0	103	2
B-1, 3.7-meter, 70°	6202	0	82, 102*	2
B-1, 6-meter, 70°	2190	0	49	2

*Coalescence of two sets of natural modes occurs near the same dynamic pressure.

IV.A.3. Effect of Tension on Limit Cycle Oscillations

Limit cycle oscillations were calculated for models A-1 and B-1 with the 3-meter geometry and Piston Theory aerodynamics. Since the TPS on the HIAD is restrained with straps at the trailing edge, it is possible that tension is applied along the axial direction. In this section, the effect of tension on the limit cycle behavior is examined. The amplitudes are normalized by the thickness of the shell, which is equivalent to the thickness of the TPS structural layer ($h = 0.000127m$). The peak limit cycle amplitudes and corresponding limit cycle frequencies as a function of dynamic pressure for model A-1 are given in Fig. 16. The dashed lines indicate the linear flutter boundaries for each value of tension. In this case, added tension is always a stabilizing effect. When the dynamic pressure is increased to twice that of the flutter boundary, the LCO amplitudes generally grow to 10-15 times the TPS shell thickness. The peak LCO frequencies always increase with dynamic pressure and the peak frequencies near the flutter boundaries are in agreement with linear theory.

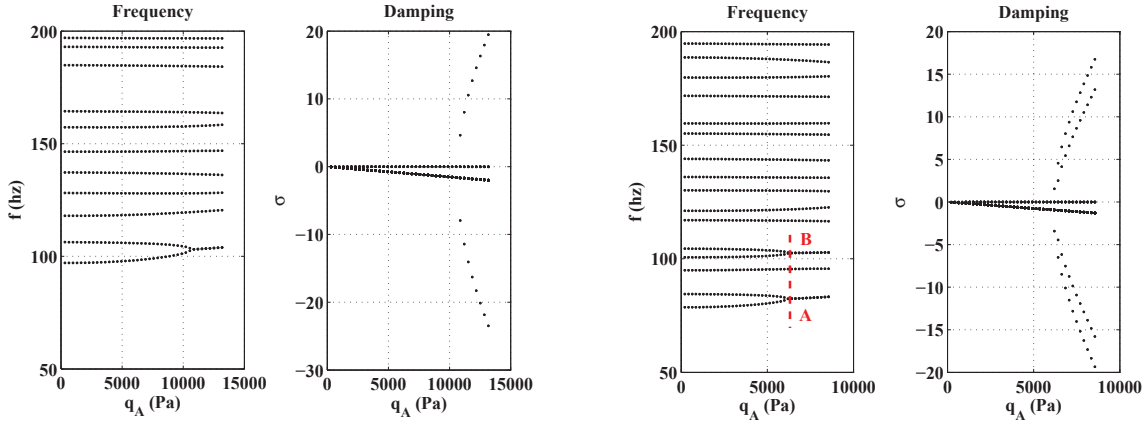

(a) 3-meter (b) 3.7-meter

Figure 15: Frequencies and system damping as a function of dynamic pressure for the 3-meter and 3.7-meter geometries, M=2.

The peak limit cycle amplitudes and corresponding limit cycle frequencies as a function of dynamic pressure for model B-1 are given in Fig. 17. The linear analysis in Part I[1] indicated a non-monotonic increase in the flutter dynamic pressure with tension due to transitions between the critical axial and circumferential modes. Consistent with the linear analysis, the LCO amplitudes decreased when 250 N/m and 750 N/m tension was applied. Unlike the single shell, increasing tension is not always a stabilizing effect in this case. The frequency response is broad spectrum at high tension values and the peak frequencies depend on the position along the shell surface. The peaks in the response are relatively constant for most tensions but the frequency spectra broaden with increasing dynamic pressure.

IV.A.4. Pre-Buckled Flutter Analysis using Piston Theory - Model B-1, 3.7-Meter Configuration

CFD simulations of a 3.7-meter HIAD[11] indicated that both the static pressure load and dynamic pressure on the surface of the vehicle peak at approximately 1000 Pa. This static load is below the nonlinear buckling load, so the shell is in a stressed but pre-buckled state. To determine the worst case scenario for flutter, both the initial static deformation and membrane forces due to the static load are included in the aeroelastic simulation. To allow for the possibility of buckling, modal expansions in the circumferential direction include both the critical buckling mode ($n = 37$) and the critical flutter mode ($n = 0$) calculated using linear theory. The nonlinear flutter calculation begins by artificially increasing the aerodynamic damping, neglecting aerodynamic stiffness terms in the equations of motion, and applying the static load. The transient oscillations decay rapidly, resulting in constant static deformation of the shell. The aerodynamic damping is then increased to the physical in-flight value, the aerodynamic stiffness terms are included, and the system is perturbed. When the CFD flight conditions are reproduced in the simulation, the oscillations decay with time and the shell remains stable. This is illustrated by the deflection time history in Fig. 18. When the dynamic pressure is increased to 2000 Pa, the oscillations grow with time and the flutter condition is attained. A further increase in dynamic pressure causes a rapid increase in amplitude, and the circumferential buckling mode becomes equally as critical as the flutter mode. This is shown in Figs. 19 and 20. In the region of the time history labeled "A" , the oscillations remain symmetric and the shell cross section is circular. The modal decomposition in Fig. 19 (right) indicates no contribution from the buckling mode. In region "B," the buckling mode is non-zero and the shell begins to wrinkle circumferentially.

IV.A.5. Limit Cycle Amplitudes Including Pre-Buckling Load and Extended Aerodynamics

Nonlinear aeroelastic solutions were calculated for all three geometries with the pre-buckling load and extended aerodynamic model, though the calculations do not include both effects simultaneously,

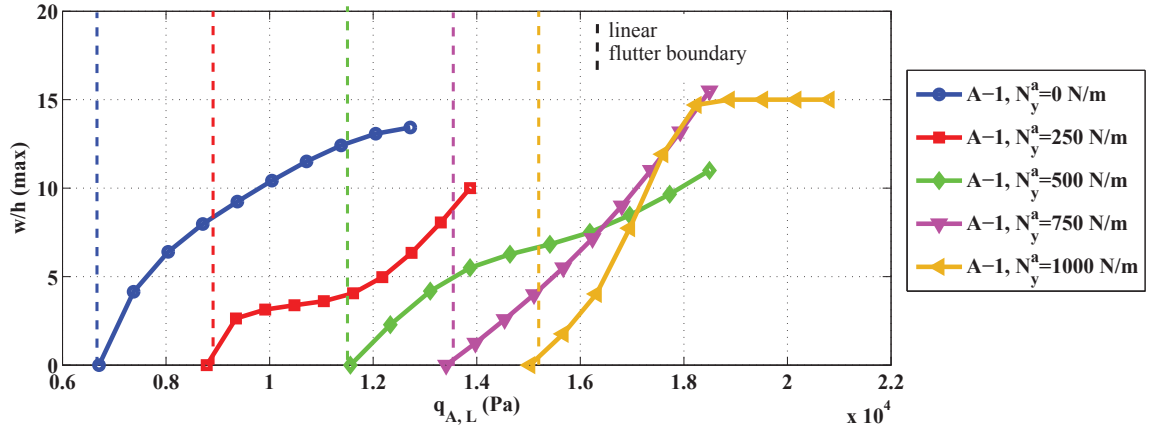

(a) Peak LCO Amplitudes.

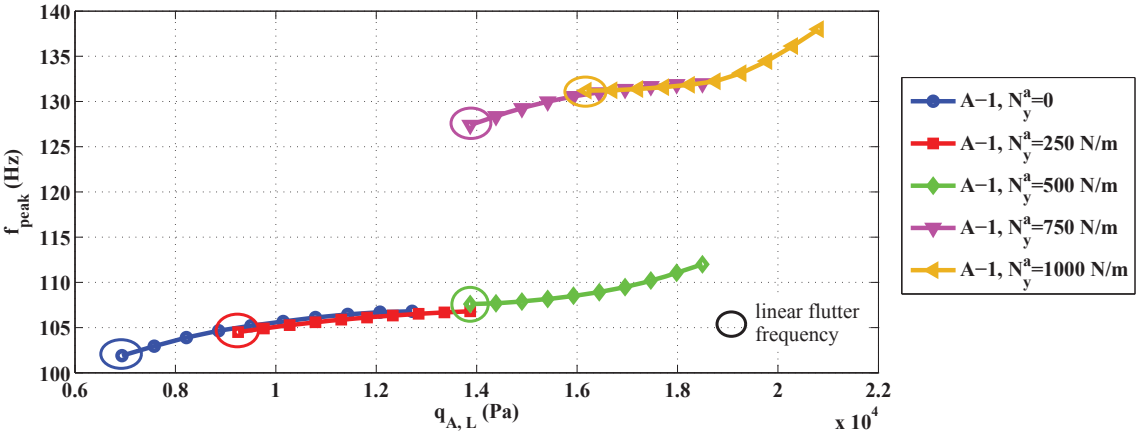

(b) Peak LCO Frequencies.

Figure 16: Effect of axial tension on the peak LCO amplitudes and frequencies for model A-1, 3-meter configuration, $M_L = 2$..

as computational cost is high. The 3.7-meter configuration is of primary concern due to possible flight applications, so a more detailed analysis will be presented for this case first. The limit cycle amplitudes as a function of dynamic pressure are given in Fig. 21a. The LCO amplitudes for the nominal cases are also included for comparison. The peak (local) dynamic pressure at peak heating of a 3.7-meter vehicle trajectory[11] is also shown at approximately 1000 Pa. The flutter onset dynamic pressures for all cases are above this point. Flutter onset for the extended aerodynamics case occurs at 4100 Pa, while the nominal case doesn't begin to flutter until 6200 Pa. When the pre-buckling load is included, amplitudes tend to increase more rapidly at higher dynamic pressures compared with the other cases. This trend is not particularly surprising, since the analysis of the pre-buckled case in the previous section indicated that at higher dynamic pressures, the shell buckles (wrinkles) circumferentially below the buckling pressure. While the shell is initially pre-buckled, it transitions to a post-buckled state with the additional aerodynamic pressure, and has a decreased ability to withstand load. This is the likely cause of the larger LCO amplitudes.

The peak limit cycle frequencies as a function of dynamic pressure for Model B-1, 3.7-meter configuration are given in Fig. 21b. Note that in many cases the frequency response above the flutter dynamic pressure is broad-spectrum and the peak frequency depends on the location on the shell surface. Near the leading edge, the frequencies are relatively high and deflections are relatively small, since this is where the shell stiffness is greatest. Near the trailing edge, the frequencies are close to the linear flutter frequency.

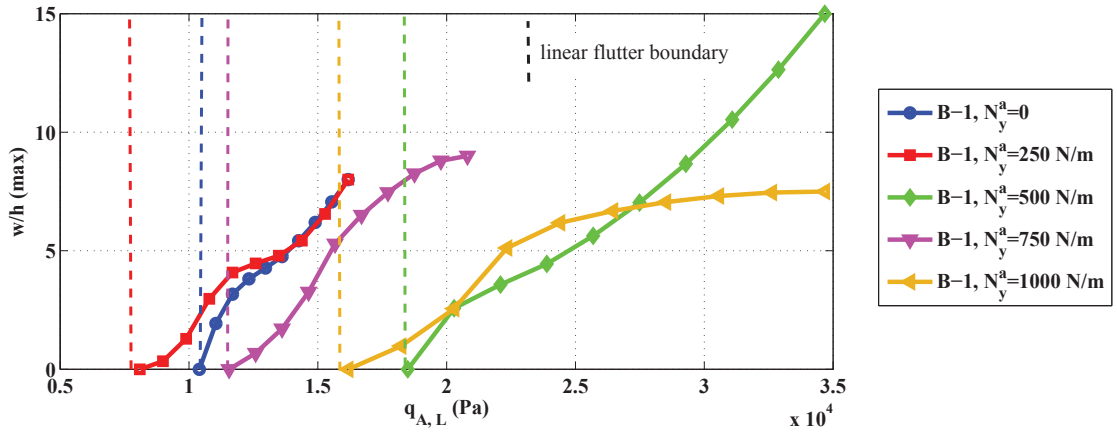

(a) Peak LCO Amplitudes.

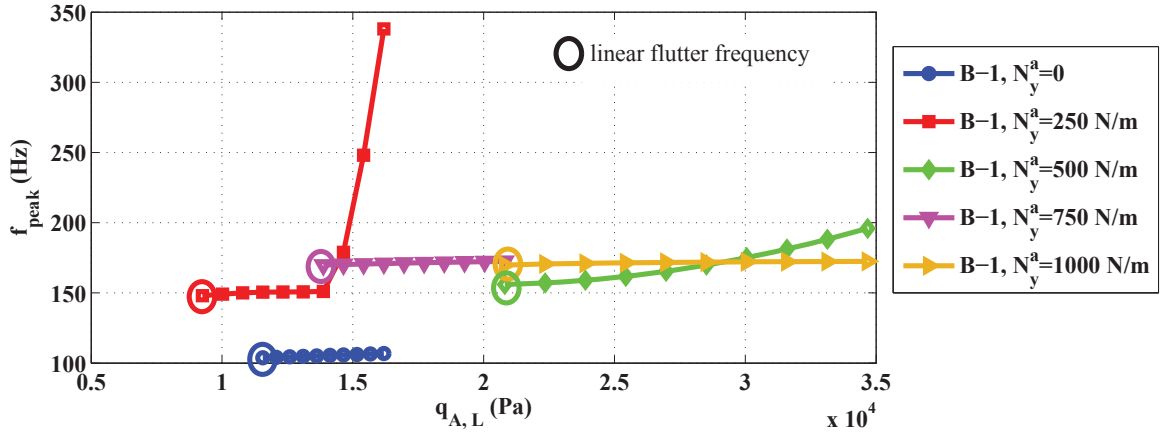

(b) Peak LCO Frequencies.

Figure 17: Effect of axial tension on the peak LCO amplitudes and frequencies for model B-1, 3-meter configuration, $M_L = 2$..

In all three cases shown, the maximum peak LCO frequency occurs at the flutter boundary, and a further increase in dynamic pressure causes a decrease in the peak frequencies to 80-86 Hz. This is not normally the case for shell flutter, since aerodynamic stiffening tends to increase the frequencies as the dynamic pressure is increased. However, the results from the linear analysis in Table 4 indicated that while the first flutter onset occurs between the 4^{th} and 5^{th} modes at 102 Hz, a second pair of modes (1 & 2) coalesce at a slightly higher dynamic pressure, with a flutter frequency of 82 Hz. Therefore, in the nonlinear response, the flutter mode involving modes 1 and 2 becomes more prominent at higher dynamic pressures. This is further demonstrated in Figs. 22 and 23. In Fig. 22, the dynamic pressures are near the flutter boundaries for each case (points labeled (1) in Fig. 21b), with peak response at 102 Hz. For the nominal case and including extended aerodynamics, additional peaks are observed near 82 Hz, but the response amplitude is lower. In Fig. 23, the dynamic pressures are well above those at the flutter boundaries (points labeled (2) in Fig. 21b), and the opposite is true, with peak response near 82 Hz and less response near 100 Hz.

The limit cycle amplitudes as a function of dynamic pressure for the 3-meter and 6-meter configurations are given in Fig. 24 and Fig. 25, respectively. The effect of extended aerodynamics on the LCO amplitudes is less pronounced in the 3-meter configuration than in both the 3.7-meter and 6-meter, though the percentage decrease in the flutter dynamic pressure compared with nominal Piston Theory is between 35 and 40 percent for all cases. The effect of the pre-buckling load is most pronounced for the 3-meter configuration, with LCO amplitudes that grow to several times the thickness at dynamic pressures only

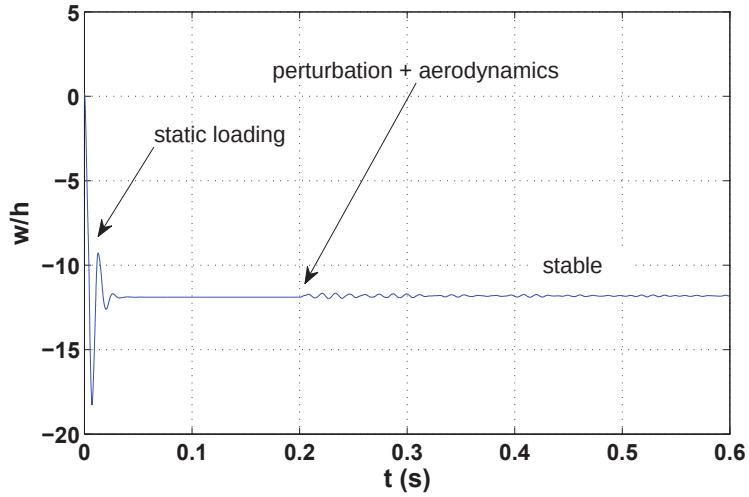

Figure 18: Deflection time history for Model B-1, 3.7-meter configuration with pre-buckling load, M=2, $q_A = 1000\ Pa$, $p_s = 1000\ Pa$ (flight condition).

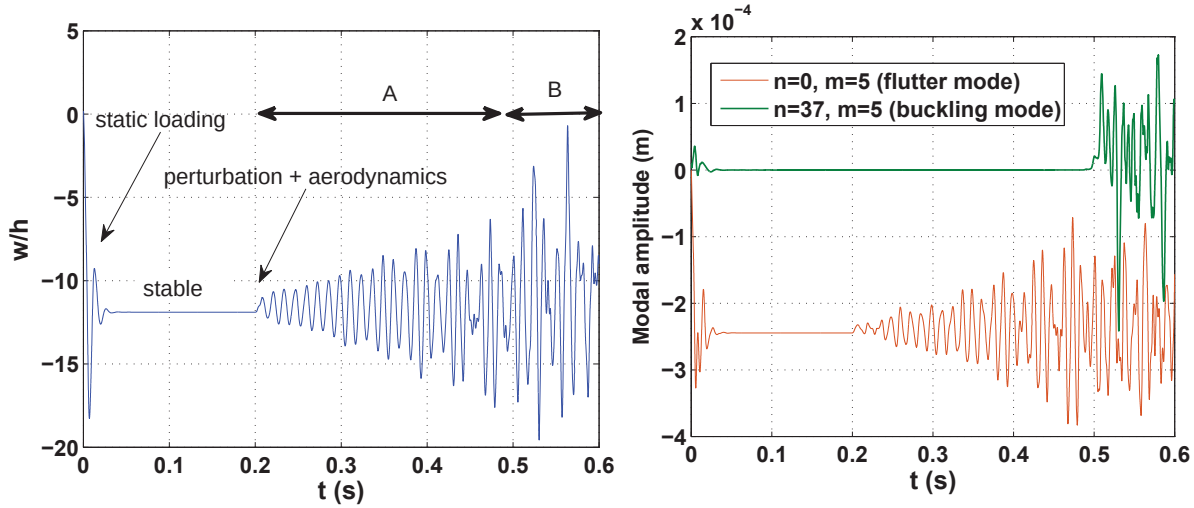

Figure 19: Deflection and modal time histories for for Model B-1, 3.7-meter configuration, $M_L = 2$, $q_A = 5000\ Pa$, $p_s = 1000\ Pa$.

slightly above the flutter boundary. The 6-meter configuration is least effected by the pre-buckling load, and the percentage decrease in the nominal flutter dynamic pressure is significantly different depending on the geometry. As a result, a new nonlinear calculation will be required to determine the flutter boundaries for different diameter shells, if the effect of pre-buckling static load is to be characterized.

V. Conclusions

A method for evaluating the nonlinear buckling and aeroelastic response of the thermal protection system on NASA's Hypersonic Inflatable Aerodynamic Decelerator has been developed using conical shell theory and potential flow aerodynamics. This method complements the linear approach used in Part I[1] of this report series by allowing for initial deformation due to static loading and the computation of limit cycle oscillations at dynamic pressures beyond the aeroelastic stability boundaries. Results have been

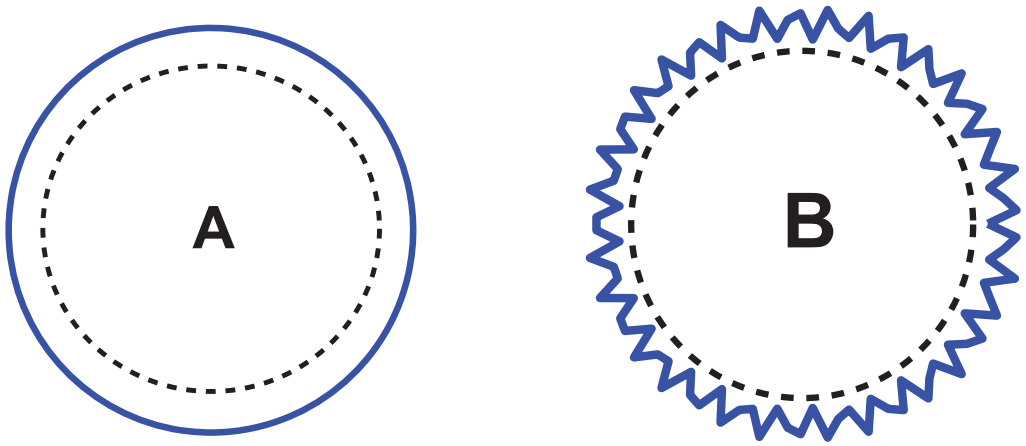

Figure 20: Circumferential flutter deflection shapes for for Model B-1, 3.7-meter configuration at times A and B, $M_L = 2$, $q_A = 5000\ Pa$, $p_s = 1000\ Pa$. The dashed line indicates the undeformed shape.

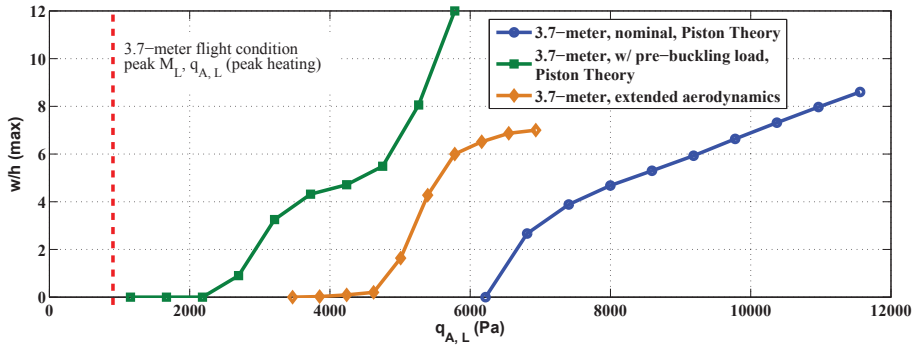

(a) Peak LCO Amplitudes.

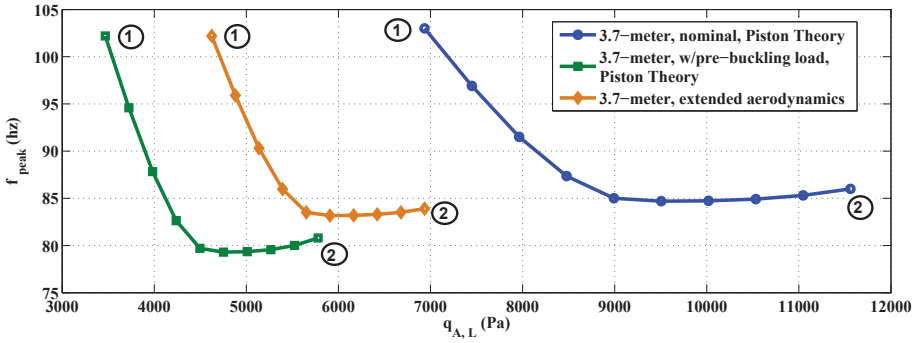

(b) Peak LCO Frequencies.

Figure 21: Peak limit cycle amplitudes and frequencies for Model B-1, 3.7-meter configuration, $M_L = 2$.

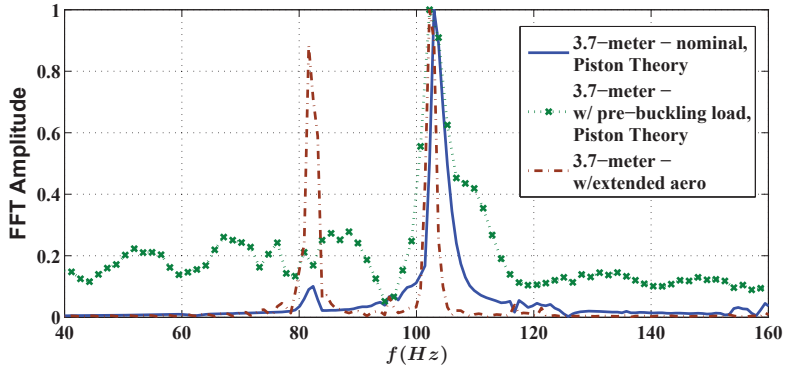

Figure 22: Frequency response for Model B-1, 3.7-meter configuration at points labeled (1), near the flutter boundaries.

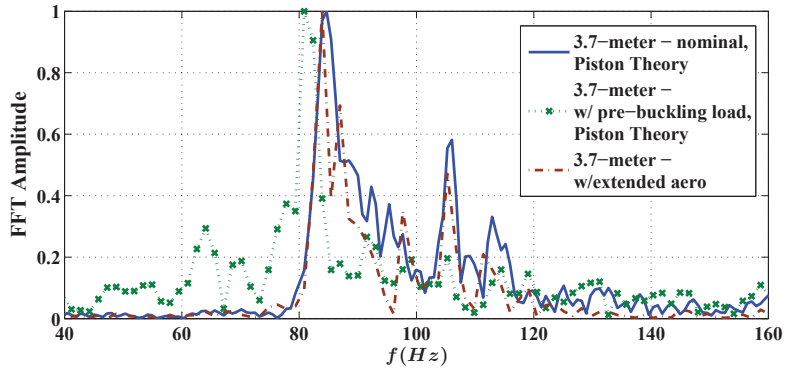

Figure 23: Frequency response for Model B-1, 3.7-meter configuration at points labeled (2), well beyond the flutter boundaries.

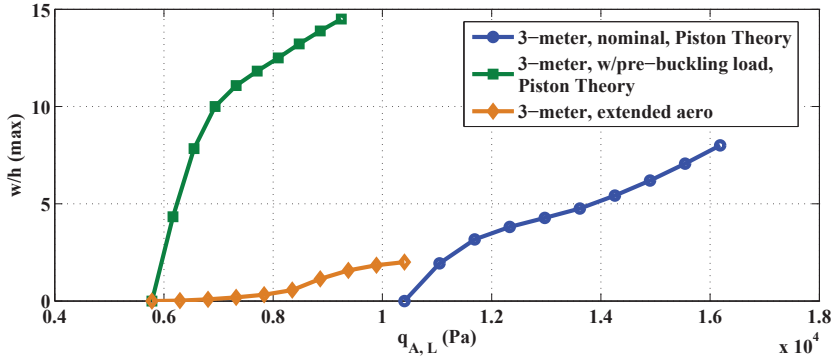

Figure 24: Limit cycle amplitudes for Model B-1, 3-meter configuration, $M_L = 2$.

computed for a TPS structural model consisting of a single conical shell resting on several circumferential elastic supports. Three conical shell geometries were considered in the present analysis: a 3-meter diameter 70° cone, a 3.7-meter 70° cone, and a 6-meter diameter 70° cone. Static load tests of a 6-meter HIAD were simulated, and theoretical strains were found to be an order of magnitude lower than experimental strains. Wrinkling of the TPS material was captured by including the critical circumferential buckling mode in the modal expansions for shell displacements, and qualitative agreement between theory and experiment was achieved. The effect of axially-applied tension was studied for a 3-meter shell, and increasing tension was generally helpful in decreasing the flutter amplitudes when the circumferen-

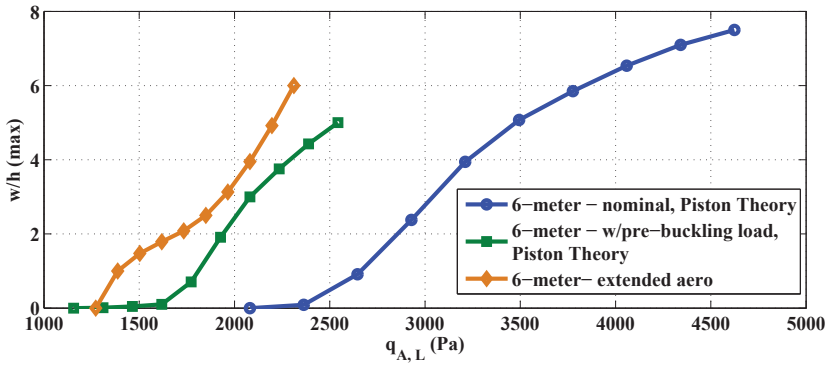

Figure 25: Limit cycle amplitudes for Model B-1, 6-meter configuration, $M_L = 2$.

tial elastic supports were ignored. Increasing tension was destabilizing in some cases when the elastic supports were included, which was consistent with previous predictions using linear theory. The effects of pre-buckling static pressure load and the extended aerodynamic model were considered for all shell geometries. When the critical circumferential buckling mode was included in the aeroelastic simulations, flutter onset began at a lower dynamic pressure and circumferential wrinkling occurred. With the extended aerodynamic model, flutter also occurred at lower dynamic pressures compared to the nominal cases with Piston Theory. The limit cycle frequencies for the 3.7-meter shell configuration exhibited unconventional behavior, as the peak frequencies decreased with increasing dynamic pressure. A linear analysis indicated that this was caused by coalescence of a second set of modes at a lower frequency, producing a flutter mode that is favored at higher dynamic pressures. The flutter boundaries predicted by all current simulations were found to be significantly higher than the local dynamic pressure calculated from CFD simulations of a proposed 3.7-meter HIAD vehicle, suggesting that for this particular geometry, flutter is not likely to occur in flight.

Appendix

Derivation of the relations between in-plane forces and static pressure loading

From cylinder theory, the axial and hoop stresses due to internal pressure are:

$$\sigma_z^{cyl} = \frac{PR}{2h} \quad \sigma_\theta^{cyl} = \frac{PR}{h} \tag{A1}$$

where R is the radius of the cylinder, h is the thickness, and P is the internal pressure. In the reference frame of the conical shell surface, these stresses become:

$$\sigma_y = \frac{\sigma_z^{cyl}}{\cos\beta} \quad \sigma_\theta = \frac{\sigma_\theta^{cyl}}{\cos\beta} \tag{A2}$$

and $R = y\sin\beta$. When the shell is subject to external pressure, let $P = -p_s$. The in-plane forces are then obtained:

$$N_y = \sigma_y h = \frac{-p_s y\tan\beta}{2} \quad N_\theta = \sigma_\theta h = -p_s y\tan\beta \tag{A3}$$

Matrix coefficients for the nonlinear conical shell models

$$A_{mnsk} = \tfrac{1}{2}\Xi^1_{nk}\int_{y_1}^{y_2}\left[\frac{E_y h}{1-\nu_\theta\nu_y}\left(\frac{d\alpha_m}{dy}\frac{d\alpha_s}{dy} + \nu_\theta\frac{1}{y}\frac{d\alpha_m}{dy}\alpha_s\right) + \frac{E_\theta h}{1-\nu_\theta\nu_y}\left(\frac{1}{y^2}\alpha_m\alpha_s + \nu_y\frac{1}{y}\frac{d\alpha_m}{dy}\alpha_s\right) + \frac{2nkG_{y\theta}h}{\sin^2\beta}\left(\frac{1}{y^2}\alpha_m\alpha_s\right)\right]ydy \tag{A4}$$

$$B_{mnsk} = \frac{1}{2}\Xi^1_{nk}\int_{y_1}^{y_2}\left[\frac{E_y h\nu_\theta}{1-\nu_\theta\nu_y}\left(\frac{1}{y}\frac{d\alpha_m}{dy}\beta_s\right) + \frac{E_\theta h}{1-\nu_\theta\nu_y}\left(\frac{2}{y^2}\alpha_m\beta_s + \nu_y\frac{1}{y}\frac{d\alpha_m}{dy}\beta_s\right) + \frac{2nG_{y\theta}h}{\sin\beta}\left(\frac{1}{y^2}\alpha_m\beta_s - \frac{2}{y}\alpha_m\frac{d\beta_s}{dy}\right)\right]ydy \tag{A5}$$

$$C_{mnsk} = \frac{1}{2}\Xi^1_{nk}\int_{y_1}^{y_2}\left[2G_{y\theta}h\left(\frac{d\beta_m}{dy}\frac{d\beta_s}{dy} - \frac{2}{y}\frac{d\beta_m}{dy}\beta_s + \frac{1}{y^2}\beta_m\beta_s\right) + \frac{nk}{\sin^2\beta}\frac{E_\theta h}{1-\nu_\theta\nu_y}\left(\frac{1}{y^2}\beta_m\beta_s\right)\right]\ ydy \tag{A6}$$

$$D_{mnsk} = \frac{1}{2}\Xi^1_{nk}\int_{y_1}^{y_2}\left[\frac{E_y h\nu_\theta\cot\alpha}{1-\nu_\theta\nu_y}\left(\frac{-1}{y}\frac{d\alpha_m}{dy}\psi_s\right) + \frac{E_\theta h\cot\alpha}{1-\nu_\theta\nu_y}\left(\frac{-2}{y^2}\alpha_m\psi_s - \nu_y\frac{1}{y}\frac{d\alpha_m}{dy}\psi_s\right)\right]ydy \tag{A7}$$

$$E_{mnsk} = \frac{1}{2}\frac{k\Xi^1_{nk}}{\sin\beta}\int_{y_1}^{y_2}\frac{E_\theta h\cot\alpha}{1-\nu_\theta\nu_y}\left(\frac{-2}{y^2}\psi_m\beta_s\right)ydy \tag{A8}$$

$$ES_{mnsk} = \frac{\Xi^1_{nk}k_s}{2}\sum_l \psi_m\psi_s y|_{y=y_l} \tag{A9}$$

$$\begin{aligned}F_{mnsk} = {}& \frac{1}{2}\Xi^1_{nk}\int_{y_1}^{y_2}\left[\frac{E_\theta h}{1-\nu_\theta\nu_y}\left(\frac{\cot^2\alpha}{y^2}\psi_m\psi_s\right) + D_y\left(\frac{d^2\psi_m}{dy^2}\frac{d^2\psi_s}{dy^2} + \nu_\theta\frac{1}{y}\frac{d\psi_m}{dy}\frac{d^2\psi_s}{dy^2}\right) + D_\theta\left(\frac{1}{y^2}\frac{d\psi_m}{dy}\frac{d\psi_s}{dy} + \nu_y\frac{1}{y}\frac{d\psi_m}{dy}\frac{d^2\psi_s}{dy^2}\right)\right]ydy\\ &+\frac{1}{2}\Xi^1_{nk}\int_{y_1}^{y_2}\left[-\frac{n^2}{\sin^2\beta}D_y\nu_\theta\left(\frac{1}{y^2}\psi_m\frac{d^2\psi_s}{dy^2}\right) - \frac{n^2}{\sin^2\beta}D_\theta\left(\frac{2}{y^3}\psi_m\frac{d\psi_s}{dy} + \nu_y\frac{1}{y^2}\psi_m\frac{d^2\psi_s}{dy^2}\right) + \frac{n^2k^2}{\sin^4\beta}D_\theta\left(\frac{1}{y^4}\psi_m\psi_s\right)\right]ydy\\ &+\frac{nk}{\sin^2\beta}\Xi^1_{nk}\int_{y_1}^{y_2}D_{y\theta}\left(\frac{1}{y^2}\frac{d\psi_m}{dy}\frac{d\psi_s}{dy} - \frac{2}{y^3}\psi_m\frac{d\psi_s}{dy} + \frac{1}{y^4}\psi_m\psi_s\right)ydy\end{aligned} \tag{A10}$$

$$G_{mnsk} = H_{mnsk} = I_{mnsk} = \frac{1}{2}M_{tot}\Xi^1_{nk}\int_{y_1}^{y_2}\psi_m\psi_s ydy \tag{A11}$$

$$\begin{aligned}J_{mnskji} = {}& \frac{1}{2}\Xi^2_{nki}\int_{y_1}^{y_2}\left[\frac{E_y h}{1-\nu_\theta\nu_y}\left(\frac{d\alpha_m}{dy}\frac{d\psi_s}{dy}\frac{d\psi_j}{dy} + \nu_\theta\frac{1}{2y}\alpha_m\frac{d\psi_s}{dy}\frac{d\psi_j}{dy}\right) + \frac{E_\theta h\nu_y}{1-\nu_\theta\nu_y}\left(\frac{1}{2y}\alpha_m\frac{d\psi_s}{dy}\frac{d\psi_j}{dy}\right)\right]ydy\\ &+\frac{1}{2}\frac{ik\Xi^3_{nki}}{\sin^2\beta}\int_{y_1}^{y_2}\left[\frac{E_y h\nu_\theta}{1-\nu_\theta\nu_y}\left(\frac{1}{2y^2}\frac{d\alpha_m}{dy}\psi_s\psi_j\right) + \frac{E_\theta h}{1-\nu_\theta\nu_y}\left(\frac{1}{y^3}\alpha_m\psi_s\psi_j + \nu_y\frac{1}{2y^2}\frac{d\alpha_m}{dy}\psi_s\psi_j\right)\right]ydy\\ &+\frac{1}{2}\frac{nki\Xi^4_{nki}}{\sin^3\beta}\int_{y_1}^{y_2}2G_{y\theta}h\left(\frac{2}{y^2}\alpha_m\frac{d\psi_s}{dy}\psi_j\right)ydy\end{aligned} \tag{A12}$$

$$\begin{aligned}K_{mnskji} = {}& \frac{1}{2}\Xi^2_{nki}\int_{y_1}^{y_2}\left[\frac{-E_y h\nu_\theta\cot\alpha}{1-\nu_\theta\nu_y}\left(\frac{1}{2y}\frac{d\psi_m}{dy}\frac{d\psi_s}{dy}\psi_j\right) - \frac{E_\theta h\nu_y\cot\alpha}{1-\nu_\theta\nu_y}\left(\frac{1}{2y}\frac{d\psi_m}{dy}\frac{d\psi_s}{dy}\psi_j\right)\right]ydy\\ &+\frac{1}{2}\frac{ik\Xi^3_{nki}}{\sin^2\beta}\int_{y_1}^{y_2} - \frac{E_\theta h\cot\alpha}{1-\nu_\theta\nu_y}\left(\frac{1}{y^3}\psi_m\psi_s\psi_j\right)ydy\end{aligned} \tag{A13}$$

$$\begin{aligned}L_{mnskji} = {}& \frac{1}{2}\frac{i\Xi^2_{nki}}{\sin\beta}\int_{y_1}^{y_2}\left[\frac{-E_y h\nu_\theta}{1-\nu_\theta\nu_y}\left(\frac{1}{2y}\frac{d\psi_m}{dy}\frac{d\psi_s}{dy}\beta_j\right) - \frac{E_\theta h\nu_y}{1-\nu_\theta\nu_y}\left(\frac{1}{2y}\frac{d\psi_m}{dy}\frac{d\psi_s}{dy}\beta_j\right)\right]ydy\\ &+\frac{1}{2}\frac{nki\Xi^5_{nki}}{\sin^3\beta}\int_{y_1}^{y_2} - \frac{E_\theta h}{1-\nu_\theta\nu_y}\left(\frac{1}{y^3}\psi_m\psi_s\beta_j\right)ydy\\ &+\frac{1}{2}\frac{k\Xi^3_{nki}}{\sin\beta}\int_{y_1}^{y_2}2G_{y\theta}h\left(\frac{2}{y^2}\frac{d\psi_m}{dy}\psi_s\beta_j - \frac{2}{y}\frac{d\psi_m}{dy}\psi_s\frac{d\beta_j}{dy}\right)ydy\end{aligned} \tag{A14}$$

$$M_{mnskjirq} = \frac{1}{2}\frac{iq\Xi^6_{nkiq}}{\sin^2\beta}\int_{y_1}^{y_2}\left[\left(\frac{E_y h\nu_\theta}{1-\nu_\theta\nu_y}+\frac{E_\theta h\nu_y}{1-\nu_\theta\nu_y}+8G_{y\theta}h\right)\left(\frac{1}{4y^2}\frac{d\psi_m}{dy}\frac{d\psi_s}{dy}\psi_j\psi_r\right)\right]ydy$$
$$+\frac{1}{2}\Xi^7_{nkiq}\int_{y_1}^{y_2}\frac{E_y h}{1-\nu_\theta\nu_y}\left(\frac{1}{4}\frac{d\psi_m}{dy}\frac{d\psi_s}{dy}\frac{d\psi_j}{dy}\frac{d\psi_r}{dy}\right)ydy \tag{A15}$$
$$+\frac{1}{2}\frac{nkiq\Xi^8_{nkiq}}{\sin^4\beta}\int_{y_1}^{y_2}\frac{E_\theta h}{1-\nu_\theta\nu_y}\left(\frac{1}{4y^4}\psi_m\psi_s\psi_j\psi_r\right)ydy$$

$$N_{mnsk} = \frac{1}{2}\frac{nk\Xi^1_{nk}}{\sin^2\beta}\int_{y_1}^{y_2}\left(\frac{\alpha_m\alpha_s}{4y^2}\right)ydy \tag{A16}$$

$$O_{mnsk} = \frac{1}{2}\frac{k\Xi^1_{nk}}{\sin\beta}\int_{y_1}^{y_2}\left(\frac{1}{2y}\frac{\partial\beta_m}{\partial y}\alpha_s+\frac{1}{2y^2}\beta_m\alpha_s\right)ydy \tag{A17}$$

$$P_m(n=0) = 2\pi\sin\beta\int_{y_1}^{y_2}\psi_m ydy \tag{A18}$$

$$PP_{mnsk} = \frac{1}{2}\Xi^1_{nk}\int_{y_1}^{y_2}\left(\frac{1}{4}\frac{\partial\beta_m}{\partial y}\frac{\partial\beta_s}{\partial y}+\frac{1}{2y}\beta_m\frac{\partial\beta_s}{\partial y}+\frac{1}{4y^2}\beta_m\beta_s\right)ydy \tag{A19}$$

$$\begin{aligned} Q^{A1}_{mnsk} &= \Xi^1_{nk}\textstyle\int_{y_1}^{y_2}\psi_m\frac{\partial\psi_s}{\partial y}ydy \\ Q^{A2}_{mnsk} &= \Xi^1_{nk}\textstyle\int_{y_1}^{y_2}\psi_m\psi_s dy \\ Q^{A3}_{mnsk} &= \Xi^1_{nk}\textstyle\int_{y_1}^{y_2}\psi_m\psi_s ydy \end{aligned} \tag{A20}$$

$$QQ_{mnsk} = \frac{1}{2}\Xi^1_{nk}\int_{y_1}^{y_2}\left(\frac{\cot^2\beta}{y^2}\beta_m\beta_s\right)ydy \tag{A21}$$

$$R_{mnsk} = \frac{1}{2}\frac{k\Xi^1_{nk}\cot\beta}{\sin\beta}\int_{y_1}^{y_2}\left(\frac{1}{2y^2}\beta_m\alpha_s\right)ydy \tag{A22}$$

$$S_{mnsk} = \frac{1}{2}\frac{nk\Xi^1_{nk}}{\sin^2\beta}\int_{y_1}^{y_2}\left(\frac{\psi_m\psi_s}{y^2}\right)ydy \tag{A23}$$

$$T_{mnsk} = \frac{1}{2}\Xi^1_{nk}\int_{y_1}^{y_2}\left(\frac{\partial\psi_m}{\partial y}\frac{\partial\psi_s}{\partial y}\right)ydy \tag{A24}$$

$$\begin{aligned} \Xi^1_{nk} &= \Xi_{nk} = \begin{cases} 0, & n\neq k \\ 2\pi\sin\beta, & n=k=0 \\ \pi\sin\beta, & n=k\neq 0 \end{cases} \\ \Xi^2_{nki} &= \textstyle\int_0^{2\pi\sin\beta}\cos n\phi\cos k\phi\cos i\phi d\phi \\ \Xi^3_{nki} &= \textstyle\int_0^{2\pi\sin\beta}\cos n\phi\sin k\phi\sin i\phi d\phi \\ \Xi^4_{nki} &= \textstyle\int_0^{2\pi\sin\beta} sinn\phi\cos k\phi\sin i\phi d\phi \\ \Xi^5_{nki} &= \textstyle\int_0^{2\pi\sin\beta}\sin n\phi\sin k\phi\cos i\phi d\phi \\ \Xi^6_{nkiq} &= \textstyle\int_0^{2\pi\sin\beta}\cos n\phi\cos k\phi\sin i\phi\sin q\phi d\phi \\ \Xi^7_{nkiq} &= \frac{1}{2}\textstyle\int_0^{2\pi\sin\beta}\cos n\phi\cos k\phi\cos i\phi\cos q\phi d\phi \\ \Xi^8_{nkiq} &= \textstyle\int_0^{2\pi\sin\beta} sinn\phi\sin k\phi\sin i\phi\mathrm{sinq}\phi d\phi \end{aligned} \tag{A25}$$

$$Q^A_{mnsk} = \frac{2q_A}{M}\left[Q^{A1}_{mnsk}-\frac{1}{2Msin\beta}Q^{A2}_{mnsk}\right]\vec{c}+\frac{2q_A}{MU_\infty}Q^{A3}_{mnsk}\dot{\vec{c}} \tag{A26}$$

$$\mathbf{C\tilde{C}A} = \sum_s\sum_k\sum_j\sum_i c_{sk}c_{ji}J_{mnskji} \tag{A27}$$

$$\mathbf{C\tilde{C}B} = \sum_m \sum_n \sum_s \sum_k c_{mn} c_{sk} L_{mnskji} \tag{A28}$$

The vector $\mathbf{C\tilde{C}C}$ is composed of both second and third order nonlinear terms:

$$\mathbf{C\tilde{C}C} = \mathbf{C\tilde{C}C^2} + \mathbf{C\tilde{C}C^3} \tag{A29}$$

where

$$\begin{aligned}\mathbf{C\tilde{C}C^2} = &\sum_m \sum_n \sum_j \sum_i a_{nm} c_{ji} J_{mnskji} + \sum_m \sum_n \sum_s \sum_k a_{nm} c_{sk} J_{mnskji} + \sum_s \sum_k \sum_j \sum_i c_{sk} c_{ji} K_{mnskji} + \sum_m \sum_n \sum_j \sum_i c_{mn} c_{ji} K_{mnskji} \\ &+ \sum_m \sum_n \sum_s \sum_k c_{mn} c_{sk} K_{mnskji} + \sum_s \sum_k \sum_j \sum_i c_{sk} b_{ji} L_{mnskji} + \sum_m \sum_n \sum_j \sum_i c_{mn} b_{ji} L_{mnskji}\end{aligned} \tag{A30}$$

$$\begin{aligned}\mathbf{C\tilde{C}C^3} = &\sum_s \sum_k \sum_j \sum_i \sum_r \sum_q c_{sk} c_{ji} c_{rq} M_{mnskjirq} + \sum_m \sum_n \sum_j \sum_i \sum_r \sum_q c_{mn} c_{ji} c_{rq} M_{mnskjirq} \\ &+ \sum_m \sum_n \sum_s \sum_k \sum_j \sum_i c_{mn} c_{sk} c_{ji} M_{mnskjirq} + \sum_m \sum_n \sum_s \sum_k \sum_r \sum_q c_{mn} c_{sk} c_{rq} M_{mnskjirq}\end{aligned} \tag{A31}$$

In the MATLAB program, it is highly inefficient to compute the third order nonlinear term using loop summations within the time-integration scheme. A vectorized method has been developed using tensor mathematics, which reduces computation time significantly. The method is implemented as follows:

1. Compute the following tensor outside of the the time-integration scheme and save for later manipulation.

$$\begin{aligned}M^1 = &\sum_s \sum_k \sum_j \sum_i \sum_r \sum_q M_{mnskjirq} + \sum_m \sum_n \sum_j \sum_i \sum_r \sum_q M_{mnskjirq} \\ &+ \sum_m \sum_n \sum_s \sum_k \sum_j \sum_i M_{mnskjirq} + \sum_m \sum_n \sum_s \sum_k \sum_r \sum_q M_{mnskjirq}\end{aligned} \tag{A32}$$

2. Compute the following tensor inside the time-integration scheme:

$$\Gamma = \left(\left(\vec{c} \otimes \vec{c} \right) \otimes \left(\vec{1} \otimes \vec{c} \right) \right) \circ M^1 \tag{A33}$$

   where $\vec{1}$ is a vector of ones the same length as the modal coordinate vector $\vec{c}$. The symbol $\otimes$ is the Kroneker product and the symbol $\circ$ is the 4-dimensional Shur product.

3. Compute the third order term in the following manner (inside the time-integration scheme) :

$$\mathbf{C\tilde{C}C} = sum\left\{ \Gamma_{\alpha\beta\gamma\delta} \middle| \ \beta = 1, ..., m_{tot} n_{tot}; \gamma = 1, ..., m_{tot} n_{tot}; \ \delta = 1, ..., m_{tot} n_{tot} \right\} \quad \text{for } \alpha = 1, ...m_{tot} n_{tot} \tag{A34}$$

   The *sum* operation indicates summation of the specified tensorial dimensions and subsequent reduction in tensor order, or "tensorial collapsing." The dimensions to be collapsed here are the fourth, third, and second dimensions, indicated by δ, γ and β, respectively. No summation is performed over the index α, such that the final quantity is an $m_{tot} n_{tot} x1$-dimensional vector.

Application of the Dowell and Bliss[15] Method to the Extended Potential-Flow Aerodynamic Theory for Conical Shells

Recall the following definition:

$$\gamma = R\delta = R\left[M^2 \left(s + \frac{p}{U_\infty} \right)^2 - s^2 \right]^{1/2} \tag{A35}$$

The first term in Eq. 27 is:

$$
\begin{aligned}
-\gamma^{-1} &= \frac{-1}{R}\left[M^2\left(s+\frac{p}{U_\infty}\right)^2 - s^2\right]^{-1/2} \\
&= \frac{-1}{R}\left[M^2\left(s+\frac{p}{U_\infty}\right)^2\left(1-\frac{s^2}{M^2\left(s+\frac{p}{U_\infty}\right)^2}\right)\right]^{-1/2} \\
&= \frac{-1}{RM\left(s+\frac{p}{U_\infty}\right)}\left(1-\frac{s^2}{M^2\left(s+\frac{p}{U_\infty}\right)^2}\right)^{-1/2}
\end{aligned}
\tag{A36}
$$

It is assumed that the magnitude of the second term in the parentheses is less than 1 since U_∞ is large (for a_∞ at sea level) and $M^2 > 1$. As a result, the Binomial theorem can be applied. Singularities do exist when $s = -p/U_\infty$, but these may be ignored by using the Fourier variable α instead of s and inverting the transform of the pressure with respect to time first, as outlined in section III.B. After applying the Binomial theorem, the first term in Eq. 27 becomes:

$$
-\gamma^{-1} \approx \frac{-1}{RM\left(s+\frac{p}{U_\infty}\right)}\left[1+\frac{s^2}{2M^2\left(s+\frac{p}{U_\infty}\right)^2}+\frac{3s^4}{8M^4\left(s+\frac{p}{U_\infty}\right)^4}+...\right] \tag{A37}
$$

Note that R is taken as constant in the initial cylindrical shell analysis, but may be a function of y when integrating to form the aerodynamic generalized forces (specifically $R = ysin\alpha$ for the conical shell).

The same procedure can be used to derive the expansions of the second and third terms in Eq. 27:

$$
\frac{1}{2}\gamma^{-2} \approx \frac{-1}{2R^2M^2\left(s+\frac{p}{U_\infty}\right)^2}\left[1+\frac{s^2}{M^2\left(s+\frac{p}{U_\infty}\right)^2}+\frac{s^4}{M^4\left(s+\frac{p}{U_\infty}\right)^4}+...\right] \tag{A38}
$$

$$
\left(\frac{n^2}{2}-\frac{3}{8}\right)\gamma^{-3} \approx \frac{\left(\frac{n^2}{2}-\frac{3}{8}\right)}{R^3M^3\left(s+\frac{p}{U_\infty}\right)^3}\left[1+\frac{3s^2}{2M^2\left(s+\frac{p}{U_\infty}\right)^2}+\frac{15s^4}{8M^4\left(s+\frac{p}{U_\infty}\right)^4}+...\right] \tag{A39}
$$

The Kernel function $A_{mnsk}(t)$ in Eq. 30, expanded with terms up to $O(1/M^5)$ is:

$$
\begin{aligned}
&A_{mnsk}(t) = \int_{-\infty}^{\infty} e^{-U_\infty i\alpha t} \times \left[\frac{-U_\infty}{8\pi^2M^3}\alpha^2 \int_{y_1}^{y_2} e^{i\alpha(y-y_1)\cos\beta}\psi_s y dy \int_{y_1}^{y_2} e^{-i\alpha(y-y_1)\cos\beta}\psi_m dy + \right. \\
&\frac{-U_\infty}{4\pi^2M^3\sin^2\beta}\left(\frac{n^2}{2}-\frac{3}{8}\right)\int_{y_1}^{y_2}\frac{e^{i\alpha(y-y_1)\cos\beta}}{y}\psi_s dy \int_{y_1}^{y_2} e^{-i\alpha(y-y_1)\cos\beta}\psi_m dy + \\
&\frac{{U_\infty}^2}{8\pi^2M^4\sin\beta}\alpha^2 t \int_{y_1}^{y_2} e^{i\alpha(y-y_1)\cos\beta}\psi_s dy \int_{y_1}^{y_2} e^{-i\alpha(y-y_1)\cos\beta}\psi_m dy + \\
&\left.\frac{3{U_\infty}^3}{16\pi^2M^5\sin^2\beta}\left(\frac{n^2}{2}-\frac{3}{8}\right)\alpha^2t^2\int_{y_1}^{y_2}\frac{e^{i\alpha(y-y_1)\cos\beta}}{y}\psi_s dy \int_{y_1}^{y_2} e^{-i\alpha(y-y_1)\cos\beta}\psi_m dy + ...\right] d\alpha
\end{aligned}
\tag{A40}
$$

Acknowledgments

The authors would like to thank the NASA Langley Aerospace Research Scholars (LARSS) program and the HIAD project for supporting this work. We also appreciate the valuable guidance of Dr. Anthony M. Calomino, Walter E. Bruce, and Dr. F. McNeil Cheatwood.

References

[1]Goldman, B. D., Dowell, E. H., and Scott, R. C., "In-Flight Aeroelastic Stability of the Thermal Protection System on the NASA HIAD, Part I: Linear Theory," *55th AIAA/ASMe/ASCE/AHS/SC Structures, Structural Dynamics, and Materials Conference*, 2014.

[2]Del Corso, J. A., Cheatwood, F., Bruce, W., Hughes, S. J., and Calomino, A. M., "Advanced High-Temperature Flexible TPS for Inflatable Aerodynamic Decelerators," *21st AIAA Aerodynamic Decelerator Systems Technology Conference and Seminar*, Vol. 1, 2011, pp. 139–161.

[3]Hughes, S. J., Cheatwood, F. M., Calomino, A. M., and Wright, H. S., "Hypersonic Inflatable Aerodynamic Decelerator (HIAD) Technology Development Overview," 2013.

[4]NASA, "HIAD Image Gallery," `http://www.nasa.gov/offices/oct/stp/game_changing_development/HIAD/images.html`.

[5]Hughes, S. J., Ware, J. S., Del Corso, J. A., and Lugo, R. A., "Deployable Aeroshell Flexible Thermal Protection System Testing," *AIAA Aerodynamic Decelerator Systems Technology Conference and Seminar, AIAA-2009-2926*, 2009.

[6]Goldman, B. D., Dowell, E. H., and Scott, R. C., "Flutter Analysis of the Thermal Protection Layer on the NASA HIAD," *Proc., 22nd AIAA Aerodynamic Decelerator Systems (ADS) Conf.*, 2013.

[7]Goldman, B. D., Scott, R. C., and Dowell, E. H., "Nonlinear Aeroelastic Analysis of the HIAD TPS Coupon in the NASA 8' High Temperature Tunnel: Theory and Experiment," *NASA TM*, , No. 2014-218267, 2014.

[8]Krumhaar, H., "The Accuracy of Linear Piston Theory When Applied to Cylindrical Shells," *AIAA Journal*, Vol. 1, No. 6, 1963, pp. 1448–1449.

[9]Seide, P., "A Donnell Type Theory for Asymmetrical Bending and Buckling of Thin Conical Shells," *Journal of Applied Mechanicsl*, Vol. 24, No. 4, 1957, pp. 761–773.

[10]MacNeal, R. H., *The NASTRAN Theoretical Manual*, Vol. 1, Scientific and Technical Information Office, National Aeronautics and Space Administration, 1972.

[11]Mazaheri, A., "70-deg IRVE on Antares Trajectory," NASA Langley Research Center.

[12]Dixon, S. C. and Hudson, M. L., *Flutter, Vibration, and Buckling of Truncated Orthotropic Conical Shells with Generalized Elastic Edge Restraint*, National Aeronautics and Space Administration, 1970.

[13]Mahmoudkhani, S., Haddadpour, H., and Navazi, H., "Supersonic Flutter Prediction of Functionally Graded Conical Shells," *Composite Structures*, Vol. 92, No. 2, 2010, pp. 377–386.

[14]Ashley, H., "Piston Theory-A New Aerodynamic Tool for the Aeroelastician," *Journal of the Aeronautical Sciences (Institute of the Aeronautical Sciences)*, Vol. 23, No. 12, 2012.

[15]Dowell, E. H. and Bliss, D. B., "New Look at Unsteady Supersonic Potential Flow Aerodynamics and Piston Theory," *AIAA Journal*, Vol. 51, No. 9, 2013, pp. 2278–2281.

[16]Bateman, H., Erdelyi, A., Magnus, W., Oberhettinger, F., and Tricomi, F., *Higher Transcendental Functions*, Vol. 2, McGraw-Hill New York, 1953.

[17]Johnson, K., "6m IS and TPS Static Load Tests," NASA Langley Research Center.

[18]Dupont, "Kevlar Technical Guide," Tech. rep., Dupont.